iScience

CellPress

Article

A SuperLEphilic/Superhydrophobic and Thermostable Separator Based on Silicone Nanofilaments for Li Metal Batteries

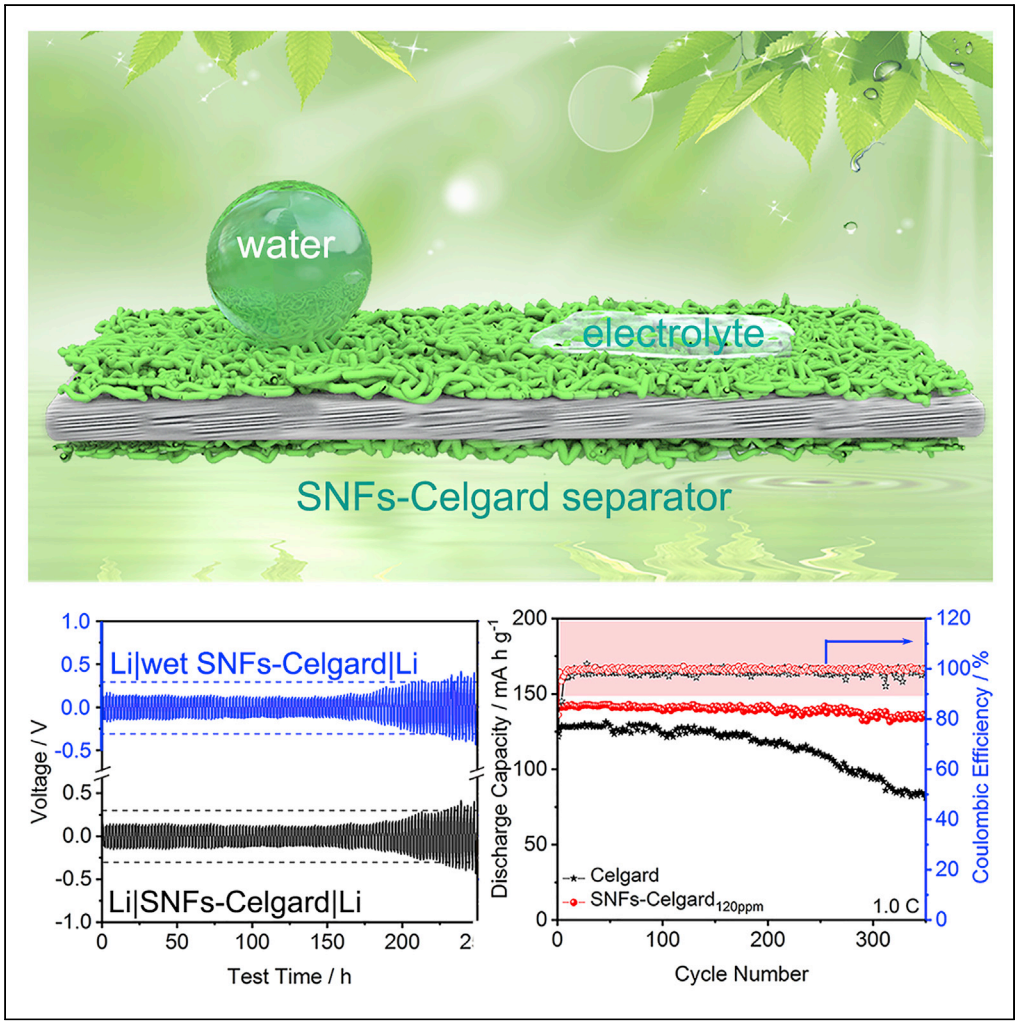

Yanfei Yang, Bucheng Li, Lingxiao Li, Stefan Seeger, Junping Zhang

jpzhang@licp.cas.cn

HIGHLIGHTS

A superLEphilic/superhydrophobic separator is first reported for Li metal batteries

The separator has low moisture uptake and could improve performance of Li/Li cells

The separator features fast LE diffusion, high LE uptake, and Li^+ conductivity

The separator could enhance performance of high-voltage Li metal batteries

Yang et al., iScience *16*, 420–432
June 28, 2019
https://doi.org/10.1016/j.isci.2019.06.010

iScience

CellPress

Article

A SuperLEphilic/Superhydrophobic and Thermostable Separator Based on Silicone Nanofilaments for Li Metal Batteries

Yanfei Yang,[1,2] Bucheng Li,[1] Lingxiao Li,[1] Stefan Seeger,[3] and Junping Zhang[1,2,4,*]

SUMMARY

Conventional polyolefin separators suffer from poor wettability to liquid electrolytes (LEs). Although some modified separators exhibit improved wettability, they are hydrophilic, causing inevitable moisture uptake. Trace water could result in poor performance and safety hazard of Li metal batteries. Here, we report a design idea of superLEphilic/superhydrophobic and thermostable separators by modifying the Celgard separator using silicone nanofilaments. The separator features low moisture uptake (~0%), fast LE diffusion (454 ms), and high LE uptake (287.8%), LE retention rate, and Li^+ conductivity. Consequently, the Li/$LiFePO_4$ cells show high cycling stability (96.05% after 350 cycles), good rate performance (125 mA h g^{-1} at 5.0 C), low resistance, and stable open circuit voltage at 160°C. Moreover, the separator could improve performance of the other Li metal batteries with high-voltage cathodes and the $LiFePO_4$/graphite pouch cells. This work provides an avenue for designing advanced separators by using bioinspired superwetting surfaces.

INTRODUCTION

Li batteries are widely used, for example, in mobile communications, portable electronic devices, and automotive technology (Seh et al., 2016; Zhang et al., 2017). However, ignition and explosion accidents of Li batteries have become more frequent recently, such as the well-known Samsung Note 7 and iPhone issues, which have caused serious safety concerns (Liu et al., 2018a). Some studies suggest that these accidents are closely related to the separator (Li et al., 2017d; Liu et al., 2018a; Palacin and de Guibert, 2016). The separator plays a key role in the capacity, cycling stability, and safety of Li batteries (Liu et al., 2018b; Lu et al., 2017). Currently, microporous polyolefin membranes are widely used as separators in commercial Li batteries because of their fascinating properties (Lu et al., 2017; Zhang et al., 2017). However, polyolefin separators show poor wettability toward liquid electrolytes (LEs) and low LE uptake (Ryou et al., 2011), which lead to low Li^+ conductivity and high internal resistance (Lee et al., 2014). Moreover, polyolefin separators exhibit inferior thermostability (Arora and Zhang, 2004; Lee et al., 2014), which may cause internal short-circuiting, ignition, and even explosion of Li batteries. These intrinsic drawbacks limit the development of advanced Li batteries (Lee et al., 2014).

To overcome these drawbacks, some efforts have been made to construct separators using materials other than polyolefins (Kim et al., 2017; Lin et al., 2016). However, these separators cannot efficiently balance all the requirements and may introduce new drawbacks, such as inferior mechanical properties (Dai et al., 2016). Considering that polyolefin separators possess many excellent properties, surface modification via coating (Dai et al., 2016; Hu et al., 2016; Ryou et al., 2011) and grafting (Abbas et al., 2017; Li et al., 2017b) is an effective approach to overcome the drawbacks. Ceramic and/or polymer coatings have been used to modify polyolefin separators (Cho et al., 2017; Jeon et al., 2016). Despite improvements in wettability and thermostability, the coatings show defects, including blocked pores, increased thickness, and reduced Li^+ conductivity, which cause serious performance degradation of Li batteries. In contrast, surface grafting of functional groups and/or polymers could minimize the thickness increase and maintain the microporous structure (Yu et al., 2016). Although the modified polyolefin separators show improved wettability and thermostability, they are also hydrophilic (Chen et al., 2016; Dai et al., 2016; Ryou et al., 2011). Thus, moisture uptake is inevitable during the use and storage periods, which is unfavorable for the assembly and performance of Li batteries, especially for Li metal batteries. At present, Li metal anode is receiving great attention owing to its highest theoretical specific capacity (3,860 mA h g^{-1}) and lowest redox potential (−3.04 V versus standard hydrogen electrode) (Cha et al., 2018; Fan et al., 2018; Liu et al., 2017). However, the uncontrollable dendrite Li growth in Li metal batteries caused many issues, such as low Coulombic

[1]Center of Eco-material and Green Chemistry, Lanzhou Institute of Chemical Physics, Chinese Academy of Sciences, Lanzhou 730000, P.R. China

[2]Center of Materials Science and Optoelectronics Engineering, University of Chinese Academy of Sciences, Beijing 100049, China

[3]Department of Chemistry, University of Zurich, Zurich 8057, Switzerland

[4]Lead Contact

*Correspondence: jpzhang@licp.cas.cn

https://doi.org/10.1016/j.isci.2019.06.010

efficiency, poor cycling stability, and safety hazard, which are the huge barriers to their real-world applications (Li et al., 2018a, 2018c; Xu et al., 2018). In fact, trace water could be involved in side reactions at the interface of electrodes (Li et al., 2018c). For example, even if there is trace water in Li metal batteries, the exothermal reactions between Li metal and water will not only induce consumption of Li anode and LEs but also accelerate dendrite Li growth, resulting in poor performance and serious safety hazard of Li metal batteries. Furthermore, the exothermal reactions may trigger diverse safety issues of Li metal batteries, such as shrinkage of the separator, ignition of the flammable separator and LE, and even explosion of batteries.

Bioinspired superhydrophobic surfaces, characterized by extremely high water repellency, have many applications, including waterproof coatings (Erbil et al., 2003), self-cleaning surfaces (Zhang et al., 2014), and oil/water separation (Li et al., 2017c). A nonfluorinated superhydrophobic surface is commonly oleophilic or superoleophilic, owing to the big difference in surface tension between water (72.8 mN m^{-1}) and most of organic liquids (<30 mN m^{-1}) (Cheng and Rodak, 2005). The surface tension of common LEs is 26.56–31.35 mN m^{-1} (Table S1). Thus, there is a great chance to prepare superLEphilic/superhydrophobic polyolefin separators for high-performance Li metal batteries. SuperLEphilic separators are defined as the separators with contact angles (CAs) of LEs close to 0°. The superLEphilicity may enhance LE uptake and retention and Li^+ conductivity owing to fast and complete wetting of the separator by LEs and thus may improve the battery performance (Lee et al., 2014). Although some LEphilic separators have been reported, superLEphilic separators are rare (Li et al., 2017a; Shi et al., 2016). The superhydrophobicity may eliminate side reactions and safety issues of Li metal batteries by reducing moisture uptake and also avoid additional trouble in battery assembly, as the drying process of separators before battery assembly is energy- and time-consuming. To the best of our knowledge, there has been no report about superLEphilic/superhydrophobic separators to date in rechargeable batteries. It is challenging to rationally design and fabricate superLEphilic/superhydrophobic separators without sacrificing other properties of polyolefin separators.

Here, we report for the first time a design idea of superLEphilic/superhydrophobic separators for Li metal batteries. The separator is prepared by growth of silicone nanofilaments (SNFs) on the surface of a polypropylene separator (Celgard 2400) by hydrolytic condensation of trichloromethylsilane (TCMS) in toluene. The microstructure of the SNFs determines wettability, LE uptake and retention, Li^+ conductivity, and thermostability of the SNFs-Celgard separator and can be tuned by the water concentration in toluene. The separator can be easily wetted by diverse LEs, and thus the LE uptake and retention and Li^+ conductivity are substantially enhanced. The separator cannot be wetted by water, and the moisture uptake is extremely low. Consequently, the performance of various Li metal batteries and the $LiFePO_4$/graphite pouch cells is evidently improved by the SNFs-Celgard separator.

RESULTS

Preparation of SNFs-Celgard Separators

Figure 1A shows the preparation of the SNFs-Celgard separator by O_2-plasma activation and subsequent SNFs growth. O_2-plasma was used to activate the chemically inert Celgard separator by forming reactive hydroxyl groups without evidently changing its microporous structure (Figure S1). Once immersed in the fresh TCMS/toluene solution containing a small amount of water, TCMS will hydrolyze and self-assemble into a highly porous polymeric network that is composed of a large amount of randomly deposited SNFs on the Celgard separator (Figures 1B and S2). The SNFs are 40–60 nm in diameter and several micrometers in length. The SNFs layer is 5.5 μm thick on each side (Figures 1C and S3), which seems to be thick. However, our previous studies have shown that the SNFs layer is soft and highly porous (Chu and Seeger, 2015; Meseck et al., 2014). The volume fraction of the SNFs layer is very low, 2.82% along the *y* axis (Meseck et al., 2014). Thus, the SNFs layer is compressible during battery assembly and the thickness of the SNFs layer in the coin cells should be ~0.155 μm on each side, assuming 100% strain of the space in the SNFs layer. The SNFs have no influence on the appearance of the Celgard separator (Figure S4). Moreover, the microstructure of the SNFs is tunable simply by the water concentration in toluene. The separators were termed as SNFs-$Celgard_{50ppm}$, SNFs-$Celgard_{120ppm}$, and SNFs-$Celgard_{200ppm}$ according to the water concentration in toluene.

In the Fourier transform infrared (FTIR) spectrum of the SNFs-Celgard separator (Figure 1D), the new absorption bands ascribed to Si-O-Si and Si-O-C stretching (1,020–1,140 cm^{-1}) and Si-CH_3 bending (1,269 and 782.9 cm^{-1}) were observed (Ward et al., 2003). In the X-ray photoelectron spectra (XPS) of the SNFs-Celgard separator (Figure 1E), the Si 2s, Si 2p, C 1s, and O 1s peaks appeared. This is in agreement

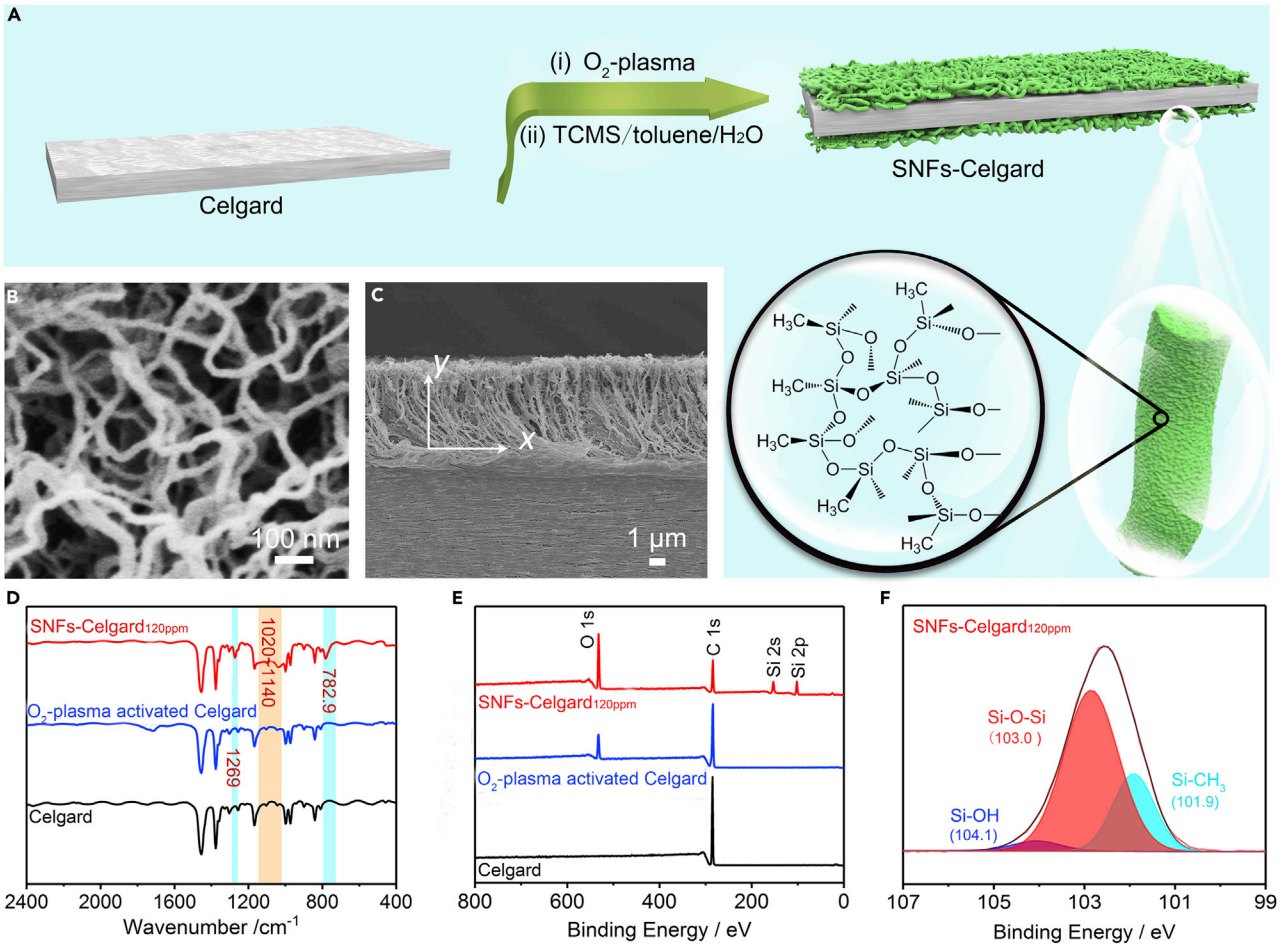

Figure 1. Preparation and Characterization of SNFs-Celgard Separators

(A) Schematic illustration of preparation of the SNFs-Celgard separator by O_2-plasma activation and subsequent SNFs growth, and chemical structure of the SNFs.

(B and C) (B) SEM and (C) cross-sectional SEM images of the SNFs-Celgard$_{120ppm}$ separator. See also Figures S2 and S3.

(D–F) (D) FTIR spectra, (E) XPS spectra, and (F) high-resolution Si 2p spectrum of the separators. See also Figure S5 and Table S2.

with the elemental maps of the separator (Figure S3B). The O/C/Si atomic ratio is 1/1.48/0.69 on the surface of the SNFs-Celgard$_{120ppm}$ separator (Table S2), which is consistent with the theoretical ratio of 1/0.66/0.66 for polymethylsilsesquioxane (Zimmermann et al., 2008). The higher C content is due to organic contamination during storage of the sample at ambient conditions in the interval between preparation and XPS analysis (Zimmermann et al., 2008). The absence of Cl 1s peak indicates complete hydrolysis of TCMS on the surface of the separator. The SNFs are mainly composed of Si-O-Si and Si-C bonds with a few Si-OH groups as demonstrated by the Si 2p spectrum of the SNFs-Celgard separator (Figure 1F) (Nozawa and Aramaki, 1999). According to the FTIR and XPS analyses, and the hydrolytic condensation of TCMS in toluene (Figure S5) (Gao and McCarthy, 2006; Zhang and Seeger, 2011b), the chemical structure of the SNFs is shown in Figure 1A.

SuperLEphilicity of SNFs-Celgard Separators

The Celgard separator is microporous with a pore diameter of several hundreds of nanometers (Figure 2A). The Celgard separator shows poor wettability toward the LE (CA_{LE} = 43.0°), which not only reduces the power density and cycle life of Li batteries but also makes the Li battery assembly time-consuming, as the LE filling is the slowest step in Li battery assembly (Arora and Zhang, 2004; Dai et al., 2016). O_2-plasma activation could make the Celgard separator LEphilic and hydrophilic. However, the CA_{water} gradually increased with storage time (Figure S6), owing to spontaneous thermal motion of the polyolefin molecular

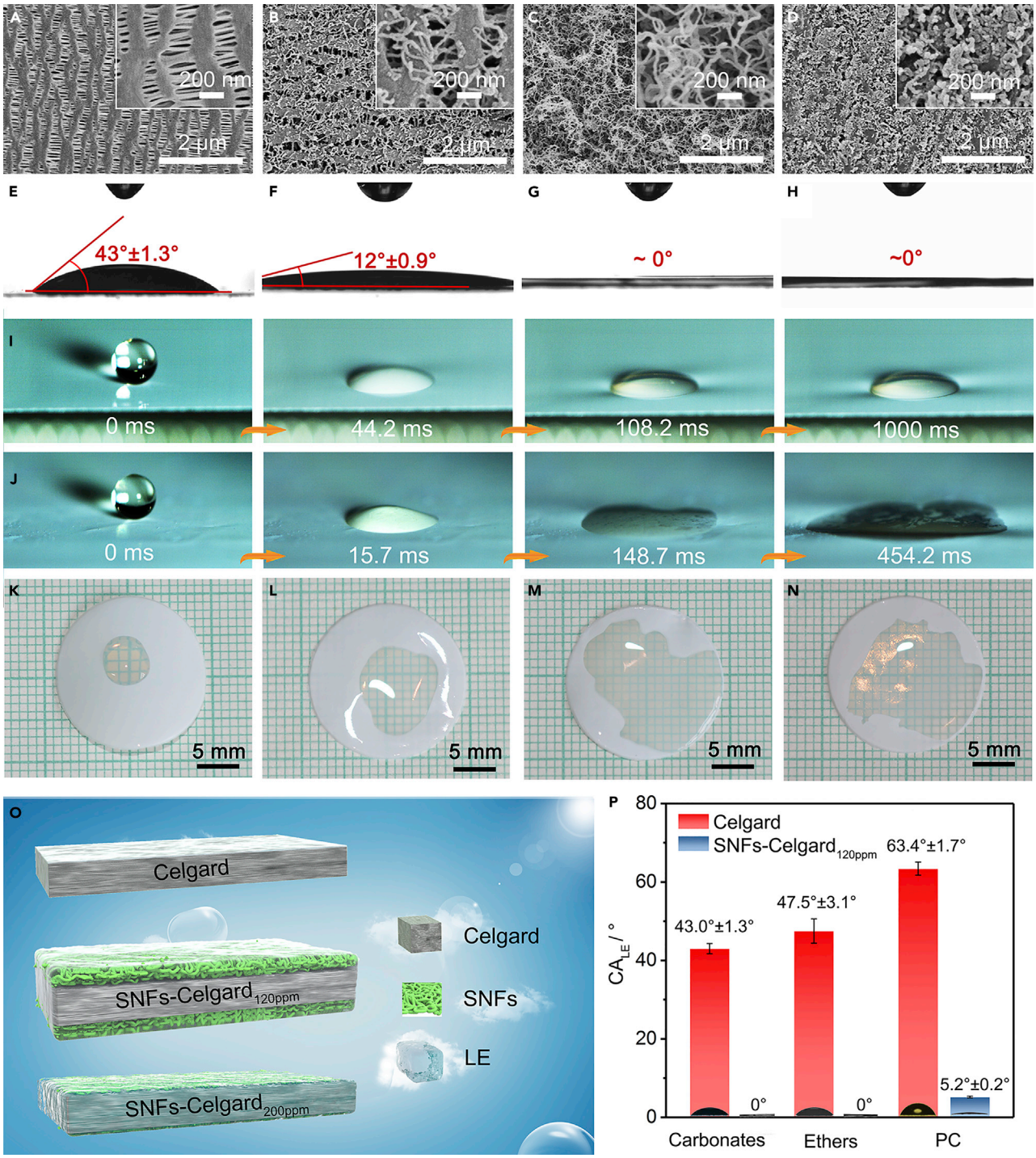

Figure 2. SuperLEphilicity of SNFs-Celgard Separators

(A–H) SEM images and CA_{LE} images of the (A and E) Celgard, (B and F) SNFs-Celgard$_{50ppm}$, (C and G) SNFs-Celgard$_{120ppm}$, and (D and H) SNFs-Celgard$_{200ppm}$ separators.

(I and J) Dynamic wetting process of the (I) Celgard and (J) SNFs-Celgard$_{120ppm}$ separators by the LE droplets (6 μL) released from a height of 5 mm. See also Videos S1 and S2.

(K–N) Photographs of the LE droplets (10 μL) after they were dropped onto the (K) Celgard, (L) SNFs-Celgard$_{50ppm}$, (M) SNFs-Celgard$_{120ppm}$, and (N) SNFs-Celgard$_{200ppm}$ separators for 10 s. See also Figures S7 and S8.

Figure 2. *Continued*

(O) Schematic illustrations of the separators with absorbed LE.

(P) CA_{LE} of the LEs with different surface tensions on the surface of the Celgard and SNFs-Celgard$_{120ppm}$ separators (shown as means ± SD, n = 6). Carbonates: 1 M $LiPF_6$ in 1:1 (v/v) EC and DMC. Ethers: 1 M LiTFSI and 0.2 M $LiNO_3$ in 1:1 (v/v) 1,2-dimethoxyethane and 1,3-dioxacyclopentane. PC: 1 M $LiPF_6$ in propylene carbonate.

chains to minimize the surface energy (Li and Zhang, 2016). After modification with TCMS at a low water concentration of 50 ppm, only sparse and short SNFs were grown on the Celgard separator (Figure 2B), because the hydrolytic condensation of TCMS could not proceed sufficiently. According to the Cassie-Baxter and the Wenzel models (Cassie and Baxter, 1944; Wenzel, 1936), introduction of a proper microstructure could make an LEphilic surface more LEphilic or even superLEphilic owing to the capillary effect (Zhang and Seeger, 2011a). Thus, the SNFs-Celgard$_{50ppm}$ separator has a smaller CA_{LE} of 12° compared with the Celgard separator (Figures 2E and 2F). Thick and long SNFs were formed upon increasing the water concentration to 120 ppm (Figure 2C), because the "vertical polymerization" of TCMS was promoted (Fadeev and McCarthy, 2000). Meanwhile, the CA_{LE} decreased to ~0° (Figure 2G), indicating formation of the superLEphilic separator. This is because the SNFs loosely stacked together and formed a 3D cross-linked polymeric network with high surface area (Meseck et al., 2014). This is further confirmed by the higher porosity of the SNFs-Celgard$_{120ppm}$ separator (51.9%) than the others (Table S3). With further increasing the water concentration to 200 ppm, a dense layer of short and worm-like SNFs was formed (Figure 2D), because the reaction was too violent. This is consistent with previous studies (Gao and McCarthy, 2006; Zhang and Seeger, 2011b). The SNFs formed at a water concentration of 200 ppm are still sufficient to make the separator superLEphilic (Figure 2H).

The dynamic wetting process of the SNFs-Celgard separators by the LE was observed using a high-speed digital camera with the Celgard separator for comparison. When dropped from a height of 5 mm onto the Celgard separator for 108.2 ms, the LE droplet reached its equilibrium state (Figure 2I and Video S1). No shape change and diffusion of the LE droplet were observed with further increasing the contact time to 1 s. In contrast, the LE droplet wetted and completely diffused into the entire SNFs-Celgard$_{120ppm}$ separator in ~454.2 ms (Figure 2J and Videos S1 and S2), owing to its superLEphilicity. This is faster than all the reported separators, including the recently reported HAP/CF separator, into which the LE droplet penetrated in 5 s (Li et al., 2017a). For the SNFs-Celgard$_{50ppm}$ and SNFs-Celgard$_{200ppm}$ separators, the LE droplets have slower diffusion speed and smaller wetting areas compared with the SNFs-Celgard$_{120ppm}$ separator (Video S1). This is because the SNFs are sparse and short. After 10 s, the LE wetting areas for the SNFs-Celgard$_{120ppm}$ and SNFs-Celgard$_{200ppm}$ separators are 1.75 and 1.61 cm^2, respectively, which are much larger than that of the SNFs-Celgard$_{50ppm}$ (0.51 cm^2) and Celgard (0.12 cm^2) separators (Figures 2K–2N). The LE filling is the slowest step in the assembly of Li batteries with the Celgard separator. Thanks to the superLEphilicity, the cell with the SNFs-Celgard$_{120ppm}$ separator can be assembled very quickly. During cell assembly, 50 μL of the LE was dripped on the surface of the separator, and the time when the separator was completely wetted was recorded. The Celgard separator was completely wetted in ~39 min, which is about 62 times more than that of the SNFs-Celgard$_{120ppm}$ separator (~37 s).

The SNFs are beneficial to enhance the LE uptake (Table S3). The LE uptake of the SNFs-Celgard$_{120ppm}$ separator is 287.8%, which is much higher than that of the SNFs-Celgard$_{200ppm}$ (196.9%), SNFs-Celgard$_{50ppm}$ (165.5%), and Celgard (91.3%) separators and the previously reported separators (80%–253%) (Dai et al., 2016; Li et al., 2017a, 2017b; Ryou et al., 2011). This is because the 3D cross-linked polymeric network of the SNFs provides a large space to accommodate the LE (Figures 2O and S3). Besides high LE uptake, the SNFs-Celgard$_{120ppm}$ separator shows high LE retention rate owing to the high affinity between the LE and the separator. After storage in room conditions for 30 min, the LE retention rate of the SNFs-Celgard$_{120ppm}$ separator is 85.6%, which is higher than that of the SNFs-Celgard$_{200ppm}$ (76.2%), SNFs-Celgard$_{50ppm}$ (67.0%), and Celgard (44.2%) separators (Figure S7). After 1 h, the Celgard separator became half dry, whereas the SNFs-Celgard$_{120ppm}$ separator was still completely wetted by the LE, demonstrating a high LE retention rate (Figure S8). It is well known that the Li^+ conductivity of a separator is closely related to the LE uptake and retention rate (Dai et al., 2016). The Li^+ conductivity of the SNFs-Celgard$_{120ppm}$ separator is 1.02 mS cm^{-1}, which is higher than that of the SNFs-Clegard$_{200ppm}$ (0.832 mS cm^{-1}), SNFs-Celgard$_{50ppm}$ (0.740 mS cm^{-1}), and Celgard (0.727 mS cm^{-1}) separators (Figure S9 and Table S3). The Li^+ conductivity was increased by 40% by introducing SNFs onto the Celgard separator. Moreover, The Si-O groups of SNFs can act as Lewis acid to trap a sufficient amount of Li salt anions (Lee et al., 2007; Wang et al., 2015), thus increasing the dissociation degree of Li salt. Consequently, the SNFs-Celgard$_{120ppm}$ separator showed

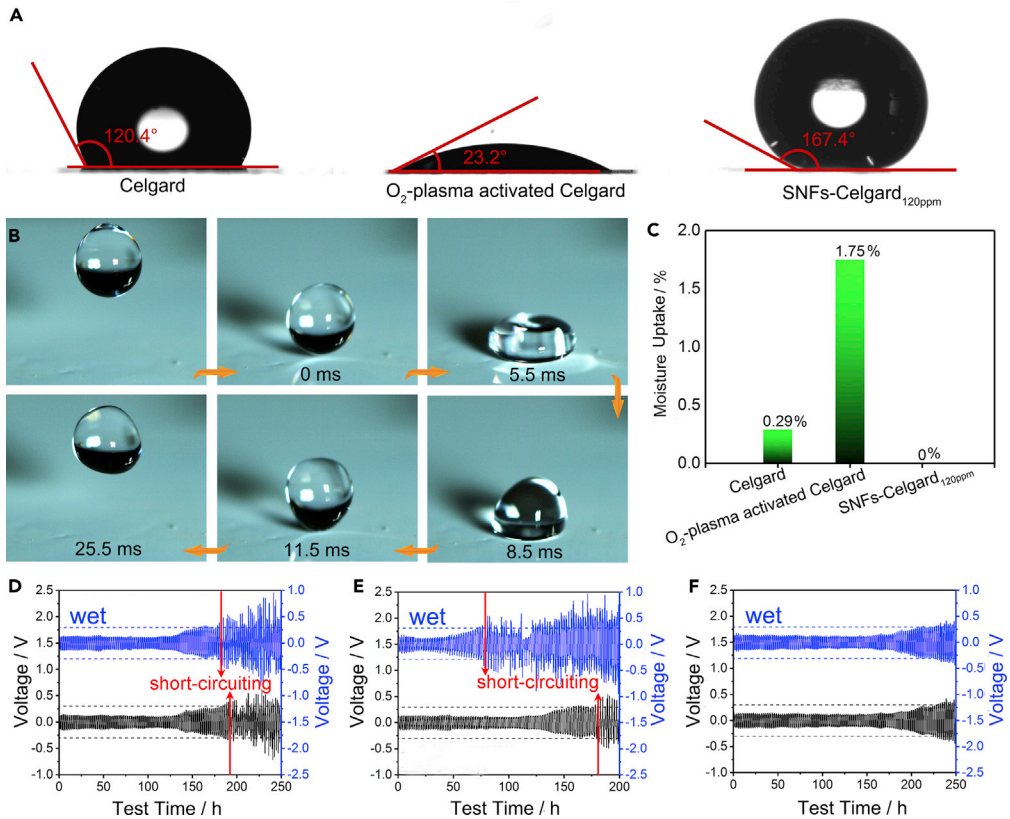

Figure 3. Superhydrophobicity of SNFs-Celgard Separators

(A) CA_{water} images of different separators.

(B) Dynamic wetting process of the SNFs-Celgard$_{120ppm}$ separator by water. See also Video S3.

(C) Moisture uptake of the separators.

(D–F) Voltage-time curves of the Li symmetric cells with the (D) Celgard, (E) O_2-plasma-activated Celgard, and (F) SNFs-Celgard$_{120ppm}$ separators. The amount of plated Li is 1.0 mA h cm^{-2}, and the current density is 1.0 mA cm^{-2} in each cycle. See also Figures S14 and S15.

higher Li^+ diffusion than the Celgard separator. To support this view, the t_{Li} was measured (Figure S10). The t_{Li} is 0.43 for the Celgard separator, which is similar to the reported data (He et al., 2018). However, the t_{Li} was significantly enhanced to 0.59 for the SNFs-Celgard$_{120ppm}$ separator.

To further demonstrate superLEphilicity of the SNFs-Celgard$_{120ppm}$ separator, three commonly used LEs with different surface tensions were studied, e.g., carbonates (27.79 mN m^{-1}), ethers (26.56 mN m^{-1}), and PC (31.35 mN m^{-1}) (Table S1). The Celgard separator showed CA_{LE} of 43.0° (carbonates), 47.5° (ethers), and 63.4° (PC), which are similar to the reported data (Hao et al., 2016; Lee et al., 2015). The SNFs-Celgard$_{120ppm}$ separator showed significantly different wettability towards these LEs (Figure 2P). The SNFs-Celgard$_{120ppm}$ separator showed CA_{LE} of ~0° for both carbonates- and ethers-based LEs, and CA_{LE} of 5.2° for the strong polar PC-based LE. After 10 s, the wetting areas of the carbonates-, ethers-, and PC-based LEs on the SNFs-Celgard$_{120ppm}$ separator are 1.75, 1.43, and 1.13 cm^2, respectively, which are much higher than those of the Celgard separator (Figure S11).

Superhydrophobicity of SNFs-Celgard Separators

Wettability of the separators towards water is shown in Figures 3A and S12. The CA_{water} is 120.4° for the Celgard separator. The CA_{water} is 23.2° for the O_2-plasma activated Celgard, as hydroxyl groups were generated on the surface of the separator. The SNFs-Celgard$_{50ppm}$ separator is close to superhydrophobic with a CA_{water} of 149.5° and a water sliding angle of 42.3°. With increasing the water concentration, the SNFs-Celgard separators became superhydrophobic. The SNFs-Celgard$_{120ppm}$ has a CA_{water} of 167.4°, and the water droplets could easily roll off the 1° tilted separator. The SNFs-Celgard$_{200ppm}$ separator

has slightly lower superhydrophobicity, as the SNFs are shorter. According to the Cassie-Baxter and the Wenzel models (Cassie and Baxter, 1944; Wenzel, 1936), introduction of a proper microstructure could make a hydrophobic surface more hydrophobic or even superhydrophobic. In addition, the methyl groups on the surface of the SNFs could decrease the surface energy of the separator, which also contributes to superhydrophobicity of the SNFs-Celgard separators. The dynamic wetting process of the SNFs-Celgard$_{120ppm}$ separator by water is shown in Figure 3B and Video S3. The 6-μL water droplet released from a height of 5 mm bounced ~14 times before settling down on the separator. The water droplet exhibited complete rebounds with a liquid-solid contact time of ~11.5 ms. These results demonstrate high superhydrophobicity of the SNFs-Celgard$_{120ppm}$ separator.

The superhydrophobicity could avoid wetting of the separator by water and may also reduce moisture uptake during the use and storage periods. This is helpful to reduce the side effects of trace water in conventional Celgard separators on the performance of Li metal batteries and additional troubles in Li metal battery assembly. To verify our hypothesis, the moisture uptake of the separators was measured by keeping the separators in a high-humidity environment (relative humidity = 92.6%, 25°C) for 7 days (Figure S13). The moisture uptake of the SNFs-Celgard$_{120ppm}$ separator is ~0% (Figure 3C). In contrast, the moisture uptake is 0.29% for the Celgard separator and is 1.75% for the O_2-plasma activated Celgard separator.

To gain more insight into the effects of the superhydrophobicity and the trace water in separators on performance of Li metal batteries, the separators after moisture uptake test (termed as wet separators) were immediately used for assembly of Li symmetric cells. In Li symmetric cells, trace water could be involved in reactions at the interface of the Li anode (Li et al., 2018c), leading to fluctuations of the voltage-time curves. For the hydrophobic Celgard separator, the polarization voltage of the cell started to increase after 135 h (Figure 3D) because of fast dendrite Li growth (Liu et al., 2017). Subsequently, a sudden drop in the polarization voltage was observed after 190 h, suggesting short-circuiting in the cell due to serious dendrite Li growth (Figure S14A). The voltage-time curve of the cell with the wet Celgard separator is stable at the beginning, but the sudden drop in the polarization voltage happened earlier (after 164 h, Figure 3D). This is because the trace water in the wet separator involved in exothermal side reactions at the interface of Li anode. These side reactions not only caused inhomogeneous solid electrolyte interphase (SEI)- formation but also accelerated dendrite Li growth and Li anode pulverization (Figure S14) and ultimately resulted in earlier failure of the cell. For the hydrophilic O_2-plasma activated separator, the voltage-time curve of the cell with the wet separator is very unstable compared with that with the normal one (Figure 3E). Also, a sudden drop in the polarization voltage, i.e., short-circuiting, happened after only 76 h. These phenomena are due to the high moisture uptake of the separator. In contrast, the cell with the SNFs-Celgard$_{120ppm}$ separator exhibits a very stable voltage-time curve in 208 h and slow increase in the voltage in subsequent cycles (Figure 3F). No short-circuiting was observed in 250 h, indicating higher stability and safety compared with the cell with the Celgard separator. Also, different from the wet Celgard and O_2-plasma-activated Celgard separators, the voltage-time curve of the cell with the wet SNFs-Celgard$_{120ppm}$ separator is very stable and is similar to that with the SNFs-Celgard$_{120ppm}$ separator (Figures 3D–3F). No dendrite Li and Li anode pulverization were observed on the surface of the cycled Li anode in the cells with the SNFs-Celgard$_{120ppm}$ separator or the wet one (Figure S15) owing to its superhydrophobicity. Thus, there is no need to dry the SNFs-Celgard$_{120ppm}$ separator before Li metal battery assembly, which is necessary for conventional separators. This is because the superhydrophobicity of the SNFs-Celgard$_{120ppm}$ separator can efficiently reduce moisture uptake and then avoid the side reactions at the interface of Li anode. The above-mentioned results indicate that the superhydrophobic SNFs-Celgard$_{120ppm}$ separator can improve performance of the Li metal battery and make battery assembly simpler.

Notably, the wettability of the SNFs-Celgard$_{120ppm}$ separator is significantly different from all the previously reported separators (Table S4). These separators are LEphilic, and only a few of them are superLEphilic, e.g., Al_2O_3/PI-coated PE separator (Shi et al., 2016), HAP/CF separator (Li et al., 2017a), and commercial ceramic-coated separators (Table S4). Meanwhile, all the separators can be easily wetted by water, which means high moisture uptake. However, the SNFs-Celgard$_{120ppm}$ separator is superLEphilic and superhydrophobic simultaneously.

It also can be concluded that the superLEphilicity, LE uptake and retention rate, Li^+ conductivity, and superhydrophobicity of the separators are closely related to the microstructure of the SNFs, which can be controlled simply by the water concentration in toluene during hydrolysis of TCMS.

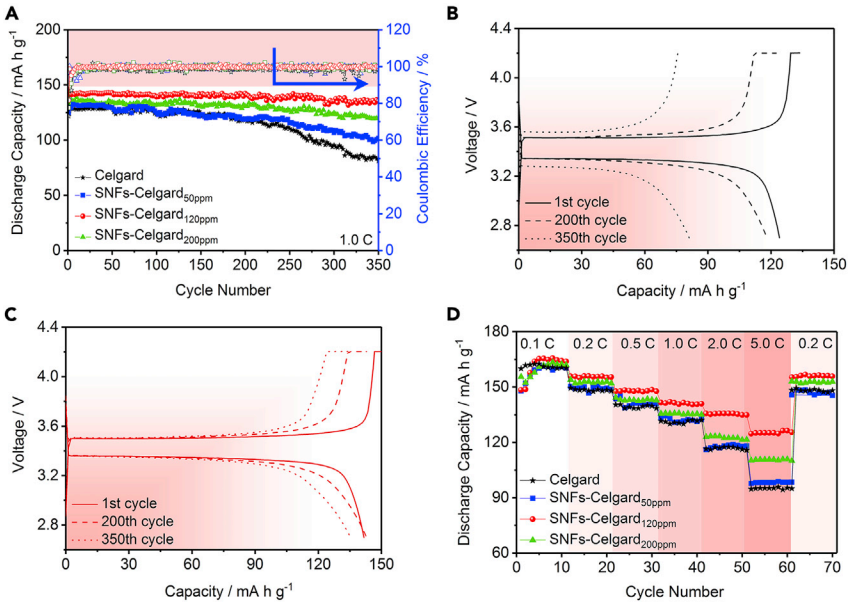

Figure 4. Electrochemical Performance of Cells with SNFs-Celgard Separators

(A) Cycling stability of the Li/$LiFePO_4$ cells with different separators.

(B and C) Discharge/charge curves of the Li/$LiFePO_4$ cells with the (B) Celgard and (C) SNFs-Celgard$_{120ppm}$ separators. See also Figure S16.

(D) Rate performance of the Li/$LiFePO_4$ cells with different separators (1 C = 160 mA h g^{-1}).

Electrochemical Performance of Cells with SNFs-Celgard Separators

The influence of the SNFs-Celgard separators on electrochemical performance of Li metal batteries was investigated using the Li/$LiFePO_4$ cells (Figure 4). The cycling stability of the cells with different separators at 1.0 C is shown in Figures 4A–4C and S16. After 350 cycles, the cells with the Celgard, SNF-Celgard$_{50ppm}$, SNFs-Celgard$_{120ppm}$, and SNFs-Celgard$_{200ppm}$ separators maintained 65.32%, 81.46%, 96.05%, and 89.77% of their initial capacity, respectively. The sharp capacity drop of the cell with the Celgard separator from the 220th cycle is ascribed to the dendrite Li growth, Li anode pulverization, and LE consumption (He et al., 2013; Liu et al., 2017). The voltage hysteresis of the cell with the Celgard separator showed an obvious increase from the 220th cycle (Figure S17), which verified LE consumption (Liu et al., 2017). Obviously, the cell with the SNFs-Celgard$_{120ppm}$ separator has the highest cycling stability, indicating that the separator could effectively alleviate the dendrite Li growth, Li anode pulverization, and LE consumption (Figures S17 and S18) (Li et al., 2018b; Ryou et al., 2012). The SNFs-Celgard$_{120ppm}$ separator is superLEphilic and has a high LE uptake and retention rate. This means the SNFs have a strong affinity to Li^+, which decreased the Li^+ concentration gradient before Li^+ reaching the Li anode surface (Cheng et al., 2016; Zhao et al., 2018). Consequently, the Li^+ distributed homogeneously over the entire Li anode surface during cycling, and the interfacial interaction between Li^+ and the Li anode was improved. It is well known that the homogeneous distribution of Li^+ is crucial to the dendrite-free Li depositing (Cheng et al., 2017). Figure S19A shows the scanning electron microscopy (SEM) image of the SNFs-Celgard$_{120ppm}$ separator after 350 cycles. The SNFs on the cycled separator is similar to those on the new one. Also, the cycled separator is still superhydrophobic (CA_{water} = 154.3°, Figure S19B). These results indicate that the SNFs-Celgard$_{120ppm}$ separator has high stability in the cyclic discharge/charge process. This is further supported by the good electrochemical stability of the SNFs-Celgard$_{120ppm}$ separator (Figure S20). This is because the Si-O groups of SNFs can act as Lewis acid to trap a sufficient amount of Li salt anions, thus delaying the irreversible oxidative decomposition of Li salt anions (Lee et al., 2007; Qiu et al., 2004; Wang et al., 2015). The gradual capacity decay of the cells with the SNFs-Celgard$_{50ppm}$ and SNFs-Celgard$_{200ppm}$ separators is because the spare or short SNFs cannot efficiently alleviate the dendrite Li growth and Li anode pulverization.

Figure 4D shows the rate performance of the Li/$LiFePO_4$ cells with different separators. At low discharge rates, e.g., 0.1 C and 0.2 C, the Li^+ conductivities of all the separators are enough to support the discharge rates and the cells displayed very similar rate performance (Dai et al., 2016). However, the

rate performance of the cells at high discharge rates is different from each other. The cell with the SNFs-Celgard$_{120ppm}$ separator has the lowest capacity loss upon cycling. At 5.0 C, the capacity is 125 mA h g^{-1}, which is 76.25% of the capacity at 0.1 C. Instead, the capacity retentions of the cells with the Celgard, SNFs-Celgard$_{50ppm}$, and SNFs-Celgard$_{200ppm}$ separators are 59.28%, 61.03%, and 68.21%, respectively. At high rates, the Li^+ conductivity and resistance act as the key factors determining the rate performance (Arora and Zhang, 2004; Dai et al., 2016). Thus, the better rate performance of the cell with the SNFs-Celgard$_{120ppm}$ separator is attributed to the higher Li^+ conductivity (Figures S10 and S11) and lower resistance (Figure S21).

The SNFs-Celgard$_{120ppm}$ separator can also be applied in the Li metal batteries with high-voltage cathode materials, such as 4.9 V $LiNi_{0.5}Mn_{1.5}O_4$ and 4.8 V $Li_{1.2}Mn_{0.54}Ni_{0.3}Co_{0.3}O_2$. Compared with the Celgard separator, the Li/$LiNi_{0.5}Mn_{1.5}O_4$ and Li/$Li_{1.2}Mn_{0.54}Ni_{0.3}Co_{0.3}O_2$ cells with the SNFs-Celgard$_{120ppm}$ separator showed higher stability in the discharge/charge process (Figures S22A and S23A), which is due to good electrochemical stability and unique wettability of the separator. Moreover, owing to higher Li^+ conductivity of the SNFs-Celgard$_{120ppm}$ separator and lower resistance of the corresponding cells (Figures S22B, S22C, S23B, and S23C), the cells showed better rate performance (Figures S22D and S23D). For the Li/$LiNi_{0.5}Mn_{1.5}O_4$ cell, the capacity decay is only 30.4% with increasing the rate from 0.1 to 1.0 C, whereas that of the cell with the Celgard separator is 37.2%. For the Li/$Li_{1.2}Mn_{0.54}Ni_{0.3}Co_{0.3}O_2$ cell, the value is 34.4% for the SNFs-Celgard$_{120ppm}$ separator and 46.3% for the Celgard separator.

To further demonstrate advantages of the SNFs-Celgard$_{120ppm}$ separator, the electrochemical performance of the Li/$LiFePO_4$ cells with the SNFs-Celgard$_{120ppm}$ separator or commercial ceramic-coated separators was compared (Figure S24). All of the separators were directly used for cell assembly. Obviously, the cycling stability and Coulombic efficiency of the cell with the SNFs-Celgard$_{120ppm}$ separator are higher and more stable than those of the cells with the ceramic-coated separators (Figure S24A). This is because the ceramic-coated separators are hydrophilic or even superhydrophilic (Figure S24B) and the water in the separators was involved in side reactions at the interface of Li anode. All of the cells showed similar interfacial resistance before cycling (Figure S24C); however, the interfacial resistance of the cells with the ceramic-coated separators increased significantly after 100 cycles (Figure S24D). This is because of exfoliation of the ceramic layer from the polyolefin membranes during cell assembly and discharge/charge, as there is no interaction between them (Lee et al., 2014).

Thermostability of SNFs-Celgard Separators

The Celgard separator has poor thermostability owing to the low melting point (Figures 5A and S25) (Arora and Zhang, 2004; Lee et al., 2014), which may cause safety issues of Li batteries (Liu et al., 2018a). Therefore, we studied the influence of the SNFs on thermostability of the separator. At temperatures above 120°C, the thermal shrinkage of the Celgard separator is evident. The sparse and short SNFs on the surface of the SNFs-Celgard$_{50ppm}$ separator did not improve the thermostability. The shrinkage of the SNFs-Celgard$_{50ppm}$ separator is similar to that of the Celgard separator at the same temperature (Figure 5B). The very thick and long SNFs on the SNFs-Celgard$_{120ppm}$ separator substantially enhanced the thermostability. The SNFs-Celgard$_{120ppm}$ separator has no visible shrinkage at temperature up to 180°C (Figures 5B and S25). However, the SNFs-Celgard$_{200ppm}$ separator starts to shrink at 170°C and has a shrinkage of 6% at 180°C, as the SNFs are very short. The high thermostability of the SNFs-Celgard$_{120ppm}$ separator was further confirmed by differential scanning calorimetry (DSC) and thermal gravimetric analysis (TGA). The endothermic peak of the SNFs-Celgard$_{120ppm}$ separator appeared at 234°C–297°C, much higher than that of the Celgard separator (160°C–220°C, Figure 5C). The evident weight loss of the Celgard separator started at 178°C, whereas that of the SNFs-Celgard$_{120ppm}$ separator started at 215°C (Figure S26). This is because the thermostable SNFs layer functioned as the thermal resistant layer to protect the Celgard separator from shrinking, like the previously reported inorganic or polymer coatings (Dai et al., 2016; Ryou et al., 2012; Yang and Zhang, 2018). Moreover, a part of TCMS molecules diffused into micropores of the Celgard separator and deposited on the wall of the micropores in the hydrolytic condensation process, forming a composite separator, which was confirmed by the cross-section elemental maps of the SNFs-Celgard$_{120ppm}$ separator (Figure S3B). This also contributes to the enhanced thermostability. It is worth noting that the Celgard separator was completely decomposed at 500°C in O_2 atmosphere, but there was ~2.40% residual SiO_2 for the SNFs-Celgard$_{120ppm}$ separator. This means the weight of the SNFs on the SNFs-Celgard$_{120ppm}$ separator is 2.68%, i.e., 0.04 mg cm^{-2}. Thus, the SNFs have negligible influence on the energy density of Li batteries.

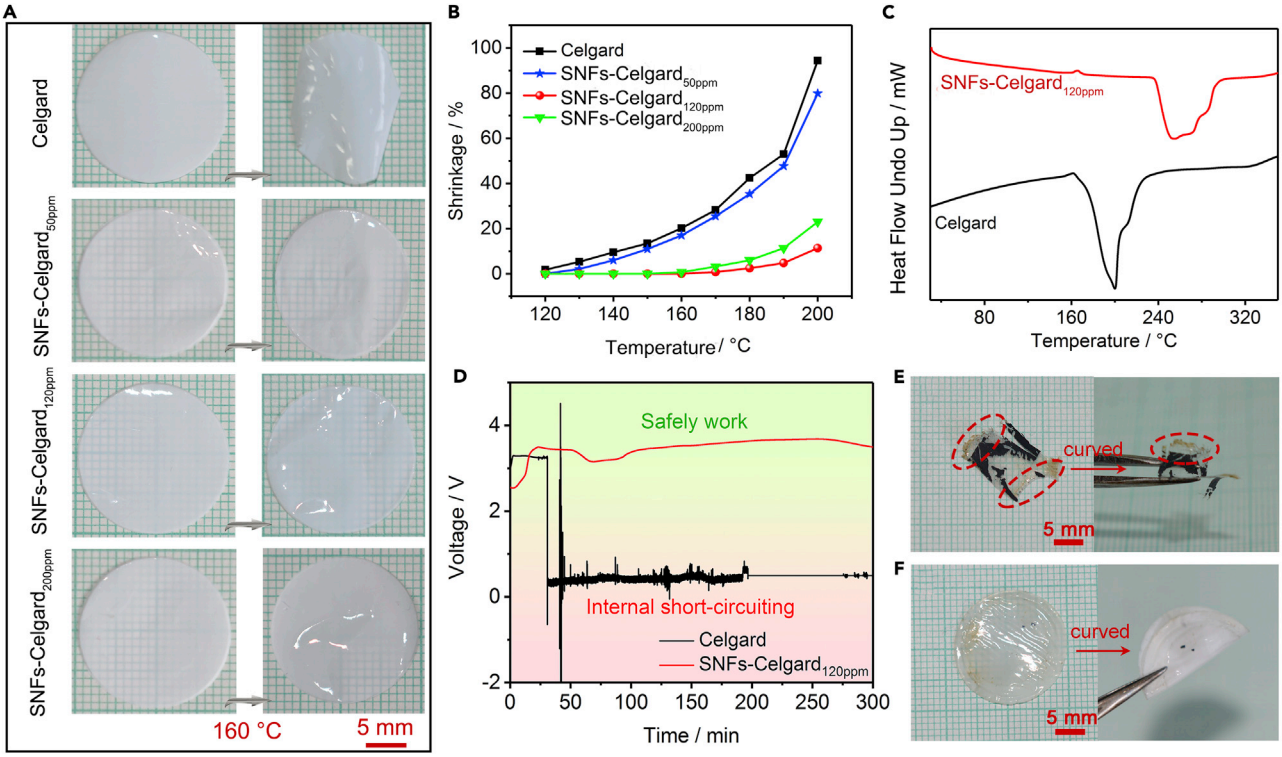

Figure 5. Thermostability of SNFs-Celgard Separators

(A) Dimensions of the separators before and after being subjected to heat treatment at 160°C for 1 h. See also Figure S25.

(B) Thermal shrinkage of the separators as a function of temperature (1 h).

(C) DSC curves of the separators. See also Figure S26.

(D) OCV curves of the Li/$LiFePO_4$ cells with different separators at 160°C.

(E and F) Photographs of the (E) Celgard and (F) SNFs-Celgard$_{120ppm}$ separators after the OCV test.

To study the effect of the SNFs-Celgard$_{120ppm}$ separator on the safety of Li metal batteries, the open circuit voltage (OCV) curves of the Li/$LiFePO_4$ cells were recorded at 160°C (Figure 5D). If there is serious thermal shrinkage of the separator, battery internal short-circuiting will result in a sudden OCV drop. For the cell with the Celgard separator, the OCV dropped sharply to 0 V after 31.5 min. However, for the cell with the SNFs-Celgard$_{120ppm}$ separator, the OCV is stable throughout the test (300 min). After the OCV test, the Celgard separator almost completely melted (Figure 5E). In contrast, the SNFs-Celgard$_{120ppm}$ separator remained intact and could still be curved without any fracture (Figure 5F). The results demonstrate that the SNFs-Celgard$_{120ppm}$ separator could evidently enhance safety of Li metal batteries.

General Applicability of SNFs-Celgard Separators

To verify applicability of the SNFs-Celgard separator in Li ion batteries, the $LiFePO_4$/graphite cells were tested. The cycling stability of the cells with different separators at 1.0 C (1.0 C = 133 mA h g^{-1}) is shown in Figure S27A. The initial discharge capacity of the cell with the SNFs-Celgard$_{120ppm}$ separator is 106 mA h g^{-1}, which is higher than those with the Celgard (94 mA h g^{-1}), SNFs-Celgard$_{50ppm}$ (98 mA h g^{-1}), and SNFs-Celgard$_{200ppm}$ (102 mA h g^{-1}) separators. After 350 cycles, the cells with the Celgard, SNF-Celgard$_{50ppm}$, SNFs-Celgard$_{120ppm}$, and SNFs-Celgard$_{200ppm}$ separators maintained 62.55%, 71.53%, 84.9%, and 79.26% of their initial capacity, respectively. The cycling stability of the cell with the SNFs-Celgard$_{120ppm}$ separator (94.3% after 100 cycles) is better than that of the cells with the Al_2O_3 ceramic-grafted separator (85.6% after 100 cycles) (Jiang et al., 2017) and the HAP/CF separator (92.3% after 100 cycles) (Li et al., 2017a). Moreover, the cell with the SNFs-Celgard$_{120ppm}$ separator showed the best rate performance compared with the other separators (Figure S27B). At 5.0 C, the capacity of the cell with the SNFs-Celgard$_{120ppm}$ separator is 58 mA h g^{-1}, which is 46.03% of the capacity at 0.1 C. Instead, the capacity retention of the cell with the Celgard separator is only 29.66%. Moreover, the

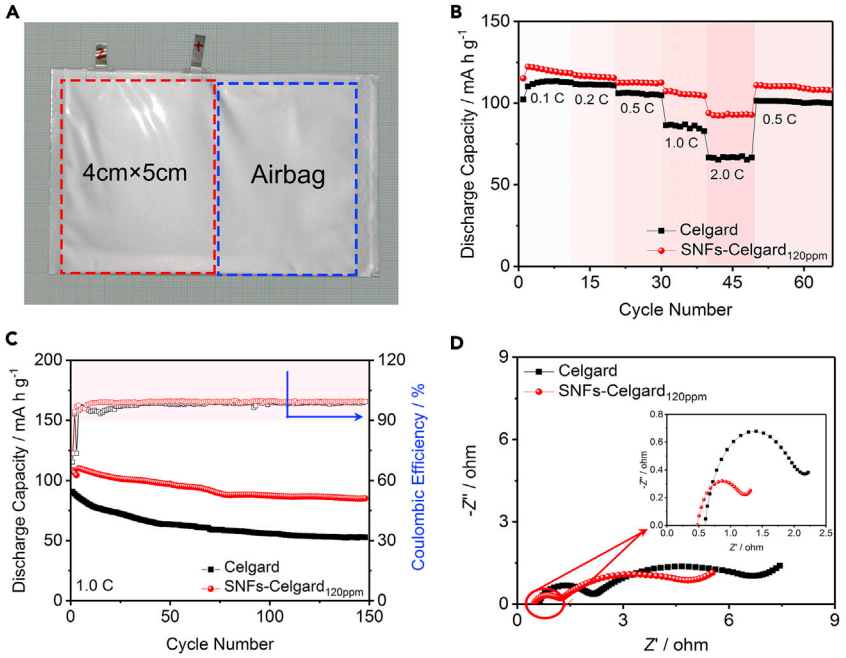

Figure 6. Electrochemical Performance of $LiFePO_4$/Graphite Pouch Cells

(A) Photograph of the pouch cell with the SNFs-Celgard$_{120ppm}$ separator.

(B–D) (B) Rate performance, (C) cycling stability at 1.0 C (1.0 C = 133 mA h g^{-1}), and (D) Nyquist plots after 150 cycles.

SNFs-Celgard$_{120ppm}$ separator could evidently enhance the safety of Li ion batteries according to the OCV curves and the photographs of the separators after the OCV test (Figure S28).

To further assess usefulness of the SNFs-Celgard$_{120ppm}$ separator in Li ion batteries, the $LiFePO_4$/graphite pouch cells with a high areal electrode loading of 2.0 mA h cm^{-2} (15.4 mg cm^{-2}) were tested (Figure 6). The capacity decay of the cell was 20.7% with increasing the rate from 0.1 to 2.0 C, whereas that of the cell with the Celgard separator reached 40.4%. The punch cell with the SNFs-Celgard$_{120ppm}$ separator also showed much better cycling stability with a capacity decay of 21.4% at 1.0 C over 150 cycles and lower resistance.

In addition, the SNFs-Celgard separator has a chance of being acceptable to the battery industry, as the cost of the SNFs layer is only ~0.11 USD m^{-2} (Table S5).

DISCUSSION

A superLEphilic/superhydrophobic and thermostable SNFs-Celgard separator was prepared by the growth of SNFs onto the Celgard separator. The superLEphilicity, LE uptake and retention rate, Li^+ conductivity, superhydrophobicity, and moisture uptake of the separator are closely related to the microstructure of the SNFs, which can be controlled simply by the water concentration in toluene. The wettability of the separator is significantly different from all the reported separators. The separator has high superLEphilicity, fast LE diffusion, high LE uptake, LE retention rate, and Li^+ conductivity. The separator also has high superhydrophobicity and low moisture uptake, making Li metal battery assembly simpler. Additionally, the separator has high thermostability. Consequently, the Li/$LiFePO_4$ cells show high cycling stability, Coulombic efficiency, rate performance, and safety, as the separator could efficiently eliminate the side reactions at the interface of Li anode triggered by trace water and could reduce resistance of the cells. In addition, the separator outperforms the commercial ceramic-coated separators in the Li/$LiFePO_4$ cells. Moreover, the separator could improve performance of the other Li metal batteries with high-voltage cathodes and the $LiFePO_4$/graphite pouch cells. We believe that this work provides an avenue for designing advanced separators for Li batteries and other metal batteries. This study also opens up a new field of application of bioinspired superwetting surfaces, like oil/water separation did a decade ago.

Limitations of the Study

The application of bioinspired superwetting surfaces on separators of Li metal batteries has not been well understood. Further in-depth study about the effects of superwetting separators on the performance of Li batteries should be carried out. In addition, the performance of the SNFs-Celgard separators was studied by using Li/$LiFePO_4$ coin cells as opposed to pouch cells. Moreover, the O_2-plasma activation technique may reduce the mechanical strength of polyolefin separators. Thus, new approaches for activation of polyolefin separators without sacrificing their inherent properties remain to be developed.

METHODS

All methods can be found in the accompanying Transparent Methods supplemental file.

SUPPLEMENTAL INFORMATION

Supplemental Information can be found online at https://doi.org/10.1016/j.isci.2019.06.010.

ACKNOWLEDGMENTS

This study was supported by the Hundred Talents Program of the Chinese Academy of Sciences, the National Natural Science Foundation of China (51503212 and 51873220), the Funds for Creative Research Groups of Gansu, China (17JR5RA306), and the Talents of Innovation and Entrepreneurship Project of Lanzhou, China (2016-RC-77).

AUTHOR CONTRIBUTIONS

Y.Y. and J.Z. conceived the concept. Y.Y. performed most of the experiments; B.L. and L.L. performed the wettability tests. All authors have thoroughly discussed the analysis of the data. Y.Y., S.S., and J.Z. wrote the manuscripts with contributions from all authors. J.Z. designed and supervised the work.

DECLARATION OF INTERESTS

The authors declare no competing interests.

Received: April 17, 2019
Revised: June 3, 2019
Accepted: June 5, 2019
Published: June 28, 2019

REFERENCES

Abbas, S.A., Ding, J., Wu, S.H., Fang, J., Boopathi, K.M., Mohapatra, A., Lee, L.W., Wang, P.C., Chang, C.C., and Chu, C.W. (2017). Modified separator performing dual physical/chemical roles to inhibit polysulfide shuttle resulting in ultra-stable Li-S batteries. ACS Nano *11*, 12436–12445.

Arora, P., and Zhang, Z.J. (2004). Battery separators. Chem. Rev. *104*, 4419–4462.

Cassie, A., and Baxter, S. (1944). Wettability of porous surfaces. Trans. Faraday Soc. *40*, 546–551.

Cha, E., Patel, M.D., Park, J., Hwang, J., Prasad, V., Cho, K., and Choi, W. (2018). 2D MoS_2 as an efficient protective layer for lithium metal anodes in high-performance Li-S batteries. Nat. Nanotechnol. *13*, 337–344.

Chen, W., Shi, L., Zhou, H., Zhu, J., Wang, Z., Mao, X., Chi, M., Sun, L., and Yuan, S. (2016). Water-based organic-inorganic hybrid coating for a high-performance separator. ACS Sustain. Chem. Eng. *4*, 3794–3802.

Cheng, Y.T., and Rodak, D.E. (2005). Is the lotus leaf superhydrophobic? Appl. Phys. Lett. *86*, 144101.

Cheng, X.B., Hou, T.Z., Zhang, R., Peng, H.J., Zhao, C.Z., Huang, J.Q., and Zhang, Q. (2016). Dendrite-free lithium deposition induced by uniformly distributed lithium ions for efficient lithium metal batteries. Adv. Mater. *28*, 2888–2895.

Cheng, X.B., Zhang, R., Zhao, C.Z., and Zhang, Q. (2017). Toward safe lithium metal anode in rechargeable batteries: a review. Chem. Rev. *117*, 10403–10473.

Cho, J., Jung, Y.C., Lee, Y.S., and Kim, D.W. (2017). High performance separator coated with amino-functionalized SiO_2 particles for safety enhanced lithium-ion batteries. J. Membr. Sci. *535*, 151–157.

Chu, Z., and Seeger, S. (2015). Multifunctional hybrid porous micro-/nanocomposite materials. Adv. Mater. *27*, 7775–7781.

Dai, J., Shi, C., Li, C., Shen, X., Peng, L., Wu, D., Sun, D., Zhang, P., and Zhao, J. (2016). A rational design of separator with substantially enhanced thermal features for lithium-ion batteries by the polydopamine-ceramic composite modification of polyolefin membranes. Energy Environ. Sci. *9*, 3252–3261.

Erbil, H.Y., Demirel, A.L., Avci, Y., and Mert, O. (2003). Transformation of a simple plastic into a superhydrophobic surface. Science *299*, 1377–1380.

Fadeev, A.Y., and McCarthy, T.J. (2000). Self-assembly is not the only reaction possible between alkyltrichlorosilanes and surfaces: monomolecular and oligomeric covalently attached layers of dichloro- and trichloroalkylsilanes on silicon. Langmuir *16*, 7268–7274.

Fan, X., Chen, L., Borodin, O., Ji, X., Chen, J., Hou, S., Deng, T., Zheng, J., Yang, C., Liou, S.C., et al. (2018). Non-flammable electrolyte enables Li-metal batteries with aggressive cathode chemistries. Nat. Nanotechnol. *13*, 715–722.

Gao, L., and McCarthy, T.J. (2006). A perfectly hydrophobic surface (θ_A/θ_R= 180/180). J. Am. Chem. Soc. *128*, 9052–9053.

Hao, X., Zhu, J., Jiang, X., Wu, H., Qiao, J., Sun, W., Wang, Z., and Sun, K. (2016). Ultrastrong polyoxyzole nanofiber membranes for dendrite-proof and heat-resistant battery separators. Nano Lett. *16*, 2981–2987.

He, H., Liu, Y., Liu, Q., Li, Z., Xu, F., Dun, C., Ren, Y., Wang, M.x., and Xie, J. (2013). Failure investigation of $LiFePO_4$ cells in over-discharge conditions. J. Electrochem. Soc. *160*, A793–A804.

He, Y., Chang, Z., Wu, S., Qiao, Y., Bai, S., Jiang, K., He, P., and Zhou, H. (2018). Simultaneously inhibiting lithium dendrites growth and polysulfides shuttle by a flexible mof-based membrane in Li-S batteries. Adv. Energy Mater. *8*, 1802130.

Hu, S., Lin, S., Tu, Y., Hu, J., Wu, Y., Liu, G., Li, F., Yu, F., and Jiang, T. (2016). Novel aramid nanofiber-coated polypropylene separators for lithium ion batteries. J. Mater. Chem. A *4*, 3513–3526.

Jeon, H., Yeon, D., Lee, T., Park, J., Ryou, M.H., and Lee, Y.M. (2016). A water-based Al_2O_3 ceramic coating for polyethylene-based microporous separators for lithium-ion batteries. J. Power Sources *315*, 161–168.

Jiang, X., Zhu, X., Ai, X., Yang, H., and Cao, Y. (2017). Novel ceramic-grafted separator with highly thermal stability for safe lithium-ion batteries. ACS Appl. Mater. Interfaces *9*, 25970–25975.

Kim, J.K., Kim, D.H., Joo, S.H., Choi, B., Cha, A., Kim, K.M., Kwon, T.H., Kwak, S.K., Kang, S.J., and Jin, J. (2017). Hierarchical chitin fibers with aligned nanofibrillar architectures: a nonwoven-mat separator for lithium metal batteries. ACS Nano *11*, 6114–6121.

Lee, J.Y., Ko, D.H., Lee, Y.M., Seol, W.H., and Park, J.K. (2007). New crosslinking agent as a Lewis acid for solid polymer electrolytes. J. Power Sources *174*, 603–606.

Lee, H., Yanilmaz, M., Toprakci, O., Fu, K., and Zhang, X. (2014). A review of recent developments in membrane separators for rechargeable lithium-ion batteries. Energy Environ. Sci. *7*, 3857–3886.

Lee, M.J., Kim, J.H., Lim, H.S., Lee, S.Y., Yu, H.K., Kim, J.H., Lee, J.S., Sun, Y.K., Guiver, M.D., Suh, K.D., et al. (2015). Highly lithium-ion conductive battery separators from thermally rearranged polybenzoxazole. Chem. Commun. (Camb.) *51*, 2068–2071.

Li, B., and Zhang, J. (2016). Durable and self-healing superamphiphobic coatings repellent even to hot liquids. Chem. Commun. (Camb.) *52*, 2744–2747.

Li, H., Wu, D., Wu, J., Dong, L.Y., Zhu, Y.J., and Hu, X. (2017a). Flexible, high-wettability and fire-resistant separators based on hydroxyapatite nanowires for advanced lithium-ion batteries. Adv. Mater. *29*, 170354.

Li, J., Huang, Y., Zhang, S., Jia, W., Wang, X., Guo, Y., Jia, D., and Wang, L. (2017b). Decoration of silica nanoparticles on polypropylene separator for lithium-sulfur batteries. ACS Appl. Mater. Interfaces *9*, 7499–7504.

Li, L., Li, B., Sun, H., and Zhang, J. (2017c). Compressible and conductive carbon aerogels from waste paper with exceptional performance for oil/water separation. J. Mater. Chem. A *5*, 14858–14864.

Li, Y., Li, Y., Pei, A., Yan, K., Sun, Y., Wu, C.L., Joubert, L.M., Chin, R., Koh, A.L., and Yu, Y. (2017d). Atomic structure of sensitive battery materials and interfaces revealed by cryo–electron microscopy. Science *358*, 506–510.

Li, L., Basu, S., Wang, Y., Chen, Z., Hundekar, P., Wang, B., Shi, J., Shi, Y., Narayanan, S., and Koratkar, N. (2018a). Self-heating-induced healing of lithium dendrites. Science *359*, 1513–1516.

Li, N., Wei, W., Xie, K., Tan, J., Zhang, L., Luo, X., Yuan, K., Song, Q., Li, H., Shen, C., et al. (2018b). Suppressing dendritic lithium formation using porous media in lithium metal-based batteries. Nano Lett. *18*, 2067–2073.

Li, S., Jiang, M., Xie, Y., Xu, H., Jia, J., and Li, J. (2018c). Developing high-performance lithium metal anode in liquid electrolytes: challenges and progress. Adv. Mater. *30*, 1706375.

Lin, D., Zhuo, D., Liu, Y., and Cui, Y. (2016). All-integrated bifunctional separator for li dendrite detection via novel solution synthesis of a thermostable polyimide separator. J. Am. Chem. Soc. *138*, 11044–11050.

Liu, Y., Liu, Q., Xin, L., Liu, Y., Yang, F., Stach, E.A., and Xie, J. (2017). Making Li-metal electrodes rechargeable by controlling the dendrite growth direction. Nat. Energy *2*, 17083.

Liu, K., Liu, Y., Lin, D., Pei, A., and Cui, Y. (2018a). Materials for lithium-ion battery safety. Sci. Adv. *4*, eaas9820.

Liu, Y., Qiao, Y., Zhang, Y., Yang, Z., Gao, T., Kirsch, D., Liu, B., Song, J., Yang, B., and Hu, L. (2018b). 3D printed separator for the thermal management of high-performance Li metal anodes. Energy Storage Mater. *12*, 197–203.

Lu, W., Yuan, Z., Zhao, Y., Zhang, H., Zhang, H., and Li, X. (2017). Porous membranes in secondary battery technologies. Chem. Soc. Rev. *46*, 2199–2236.

Meseck, G.R., Käch, A., and Seeger, S. (2014). Three-dimensional organization of surface-bound silicone nanofilaments revealed by focused ion beam nanotomography. J. Phy. Chem. C *118*, 24967–24975.

Nozawa, K., and Aramaki, K. (1999). One- and two-dimensional polymer films of modified alkanethiol monolayers for preventing iron from corrosion. Corros. Sci. *41*, 57–73.

Palacin, M.R., and de Guibert, A. (2016). Why do batteries fail? Science *351*, 1253292.

Qiu, W.L., Ma, X.H., Yang, Q.H., Fu, Y.B., and Zong, X.F. (2004). Novel preparation of nanocomposite polymer electrolyte and its application to lithium polymer batteries. J. Power Sources *138*, 245–252.

Ryou, M.H., Lee, Y.M., Park, J.K., and Choi, J.W. (2011). Mussel-inspired polydopamine-treated polyethylene separators for high-power Li-ion batteries. Adv. Mater. *23*, 3066–3070.

Ryou, M.H., Lee, D.J., Lee, J.N., Lee, Y.M., Park, J.K., and Choi, J.W. (2012). Excellent cycle life of lithium-metal anodes in lithium-ion batteries with mussel-inspired polydopamine-coated separators. Adv. Energy Mater. *2*, 645–650.

Seh, Z.W., Sun, Y., Zhang, Q., and Cui, Y. (2016). Designing high-energy lithium-sulfur batteries. Chem. Soc. Rev. *45*, 5605–5634.

Shi, C., Dai, J., Shen, X., Peng, L., Li, C., Wang, X., Zhang, P., and Zhao, J. (2016). A high-temperature stable ceramic-coated separator prepared with polyimide binder/Al_2O_3 particles for lithium-ion batteries. J. Membr. Sci. *517*, 91–99.

Wang, Z., Guo, F., Chen, C., Shi, L., Yuan, S., Sun, L., and Zhu, J. (2015). Self-assembly of PEI/SiO_2 on polyethylene separators for Li-ion batteries with enhanced rate capability. ACS Appl. Mater. Interfaces *7*, 3314–3322.

Ward, L.J., Schofield, W.C.E., and Badyal, J.P.S. (2003). Atmospheric pressure glow discharge deposition of polysiloxane and SiOx films. Langmuir *19*, 2110–2114.

Wenzel, R.N. (1936). Resistance of solid surfaces to wetting by water. Ind. Eng. Chem. *28*, 988–994.

Xu, R., Zhang, X.Q., Cheng, X.B., Peng, H.J., Zhao, C.Z., Yan, C., and Huang, J.Q. (2018). Artificial soft-rigid protective layer for dendrite-free lithium metal anode. Adv. Funct. Mater. *28*, 1705838.

Yang, Y., and Zhang, J. (2018). Highly stable lithium-sulfur batteries based on laponite nanosheet-coated celgard separators. Adv. Energy Mater. *8*, 1801778.

Yu, X., Joseph, J., and Manthiram, A. (2016). Suppression of the polysulfide-shuttle behavior in Li–S batteries through the development of a facile functional group on the polypropylene separator. Mater. Horiz. *3*, 314–319.

Zhang, J., and Seeger, S. (2011a). Polyester materials with superwetting silicone nanofilaments for oil/water separation and selective oil absorption. Adv. Funct. Mater. *21*, 4699–4704.

Zhang, J., and Seeger, S. (2011b). Superoleophobic coatings with ultralow sliding angles based on silicone nanofilaments. Angew. Chem. Int. Ed. *50*, 6652–6656.

Zhang, J., Wang, A., and Seeger, S. (2014). *Nepenthes* pitcher inspired anti-wetting silicone nanofilaments coatings: preparation, unique anti-wetting and self-cleaning behaviors. Adv. Funct. Mater. *24*, 1074–1080.

Zhang, W., Tu, Z., Qian, J., Choudhury, S., Archer, L.A., and Lu, Y. (2017). Design principles of functional polymer separators for high-energy, metal-based batteries. Small *14*, 1703001.

Zhao, C.Z., Chen, P.Y., Zhang, R., Chen, X., Li, B.Q., Zhang, X.Q., Cheng, X.B., and Zhang, Q. (2018). An ion redistributor for dendrite-free lithium metal anodes. Sci. Adv. *4*, eaat3446.

Zimmermann, J., Reifler, F.A., Fortunato, G., Gerhardt, L.C., and Seeger, S. (2008). A simple, one-step approach to durable and robust superhydrophobic textiles. Adv. Funct. Mater. *18*, 3662–3669.

ISCI, Volume *16*

Supplemental Information

A SuperLEphilic/Superhydrophobic and Thermostable Separator Based on Silicone Nanofilaments for Li Metal Batteries

Yanfei Yang, Bucheng Li, Lingxiao Li, Stefan Seeger, and Junping Zhang

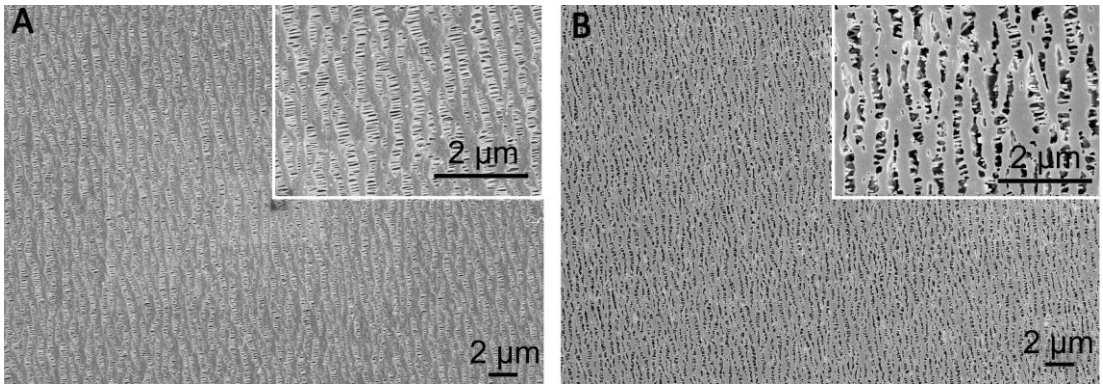

Figure S1. SEM images of the (A) Celgard and (B) O_2-plasma activated Celgard separators, related to Figure 1.

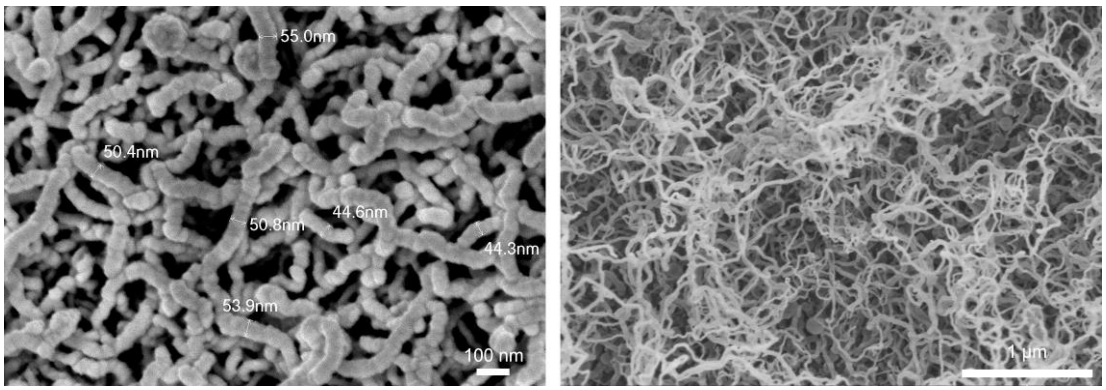

Figure S2. SEM images of the SNFs-Celgard$_{120ppm}$ separator, related to Figure 1B.

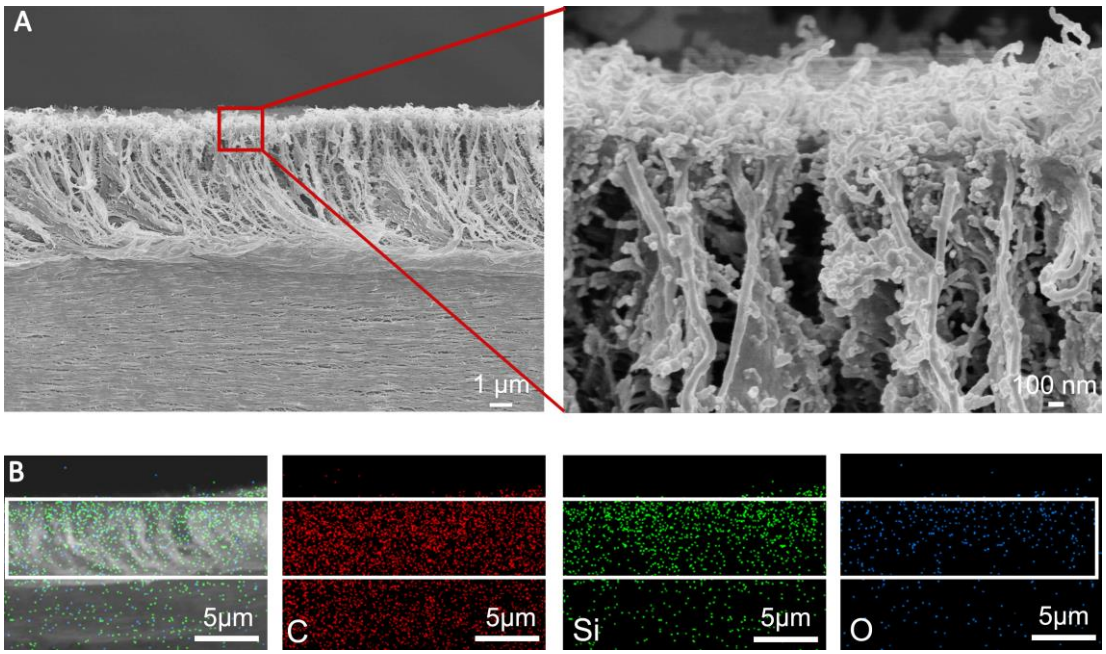

Figure S3. (A) Cross-sectional SEM images and (B) elemental maps of the SNFs-Celgard$_{120ppm}$ separator, related to Figure 1 and Figure 5.

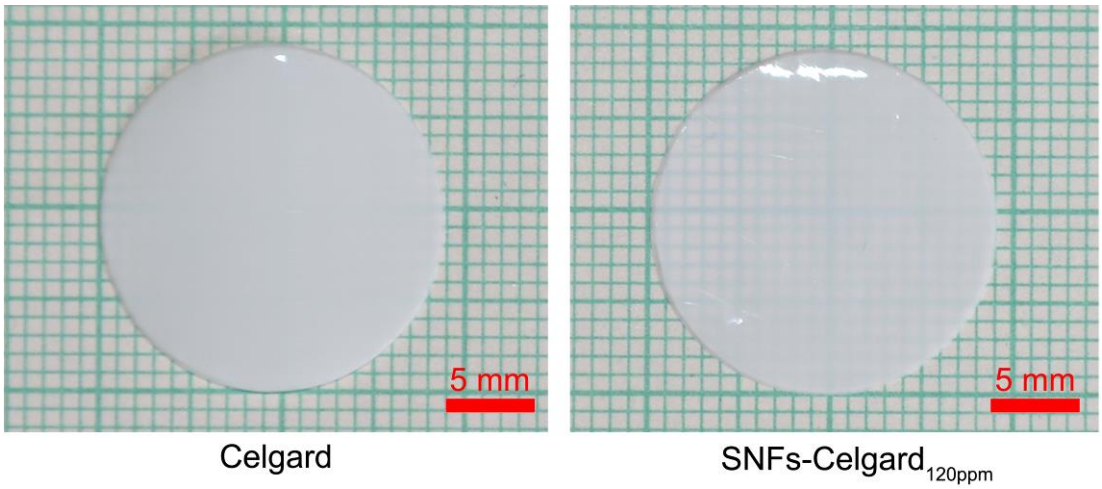

Figure S4. Photographs of the separators, related to Figure 1.

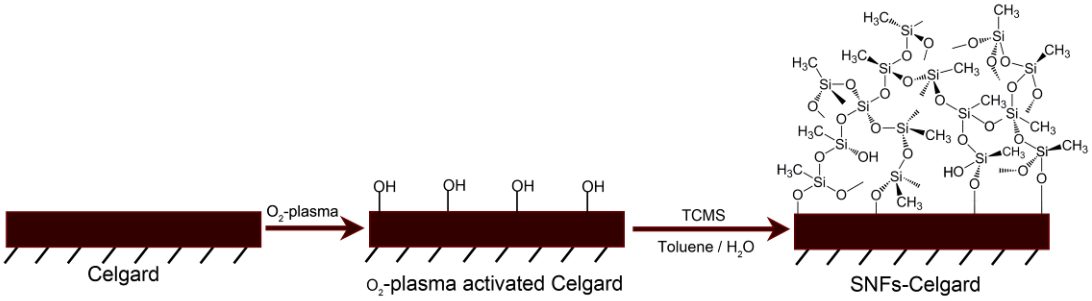

Figure S5. Synthesis of the SNFs-Celgard separator, related to Figure 1D-F.

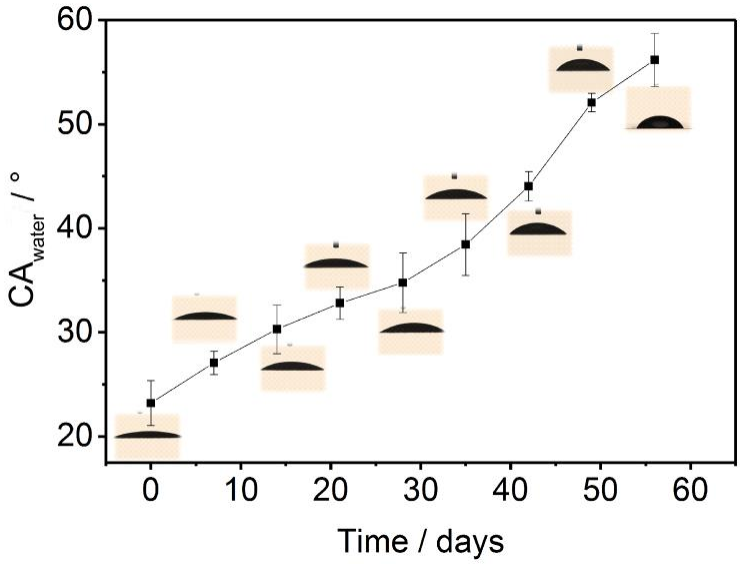

Figure S6. Variation of CA_{water} of the O_2-plasma activated Celgard separator with storage time (shown as means ± SD, n = 6), related to Figure 2F.

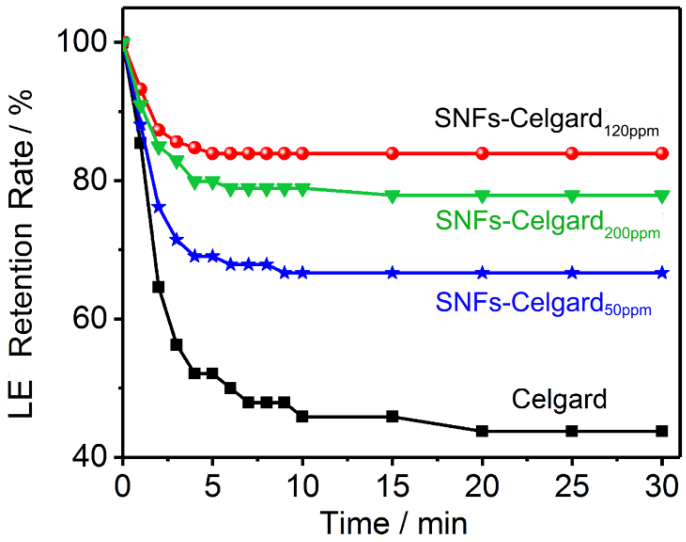

Figure S7. Variation of LE retention rate of the separators with storage time in room conditions, related to Figure 2K.

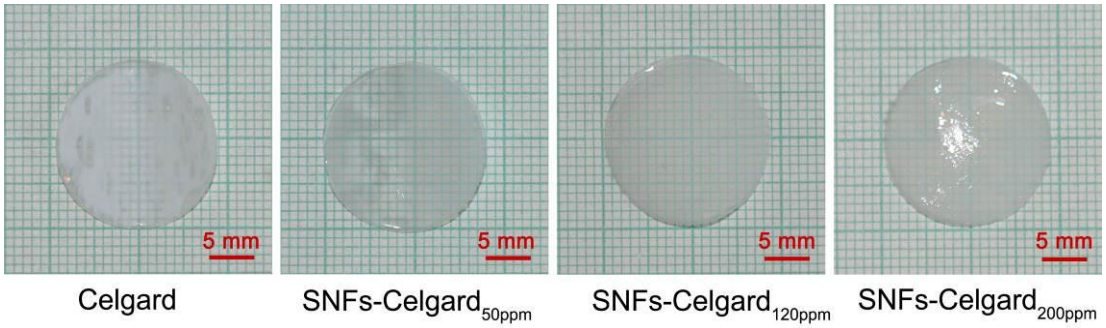

Figure S8. Photographs of the separators with absorbed LE after kept in room conditions for 1 h, related to Figure 2K.

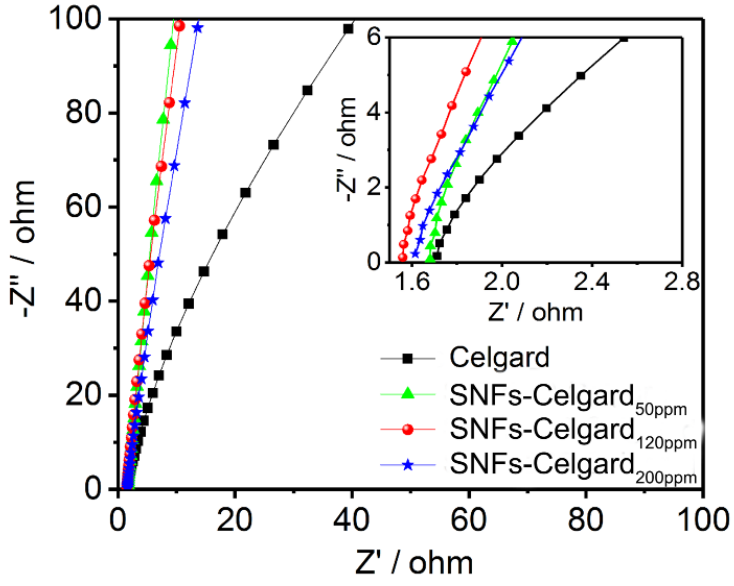

Figure S9. Impedance plots of the cells with different separators, related to Figure 2.

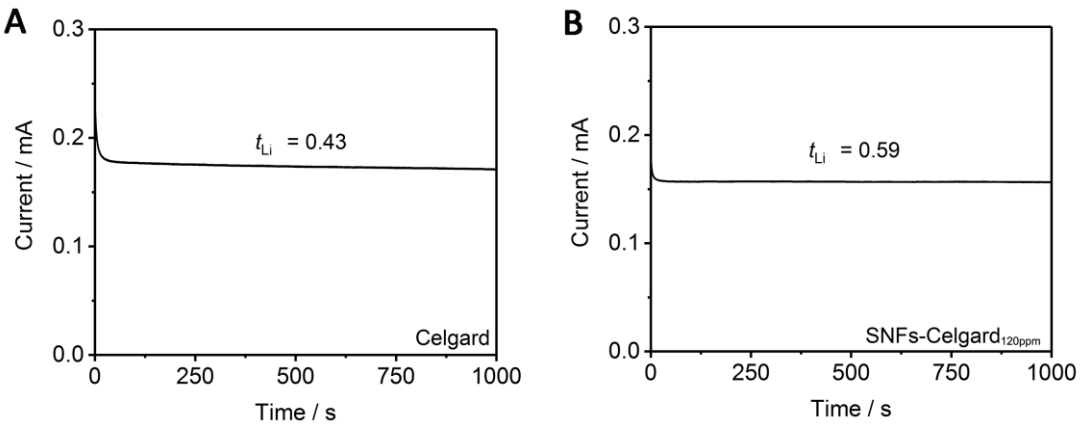

Figure S10. The characteristic of Li^+ transference number (t_{Li}), related to Figure 2.

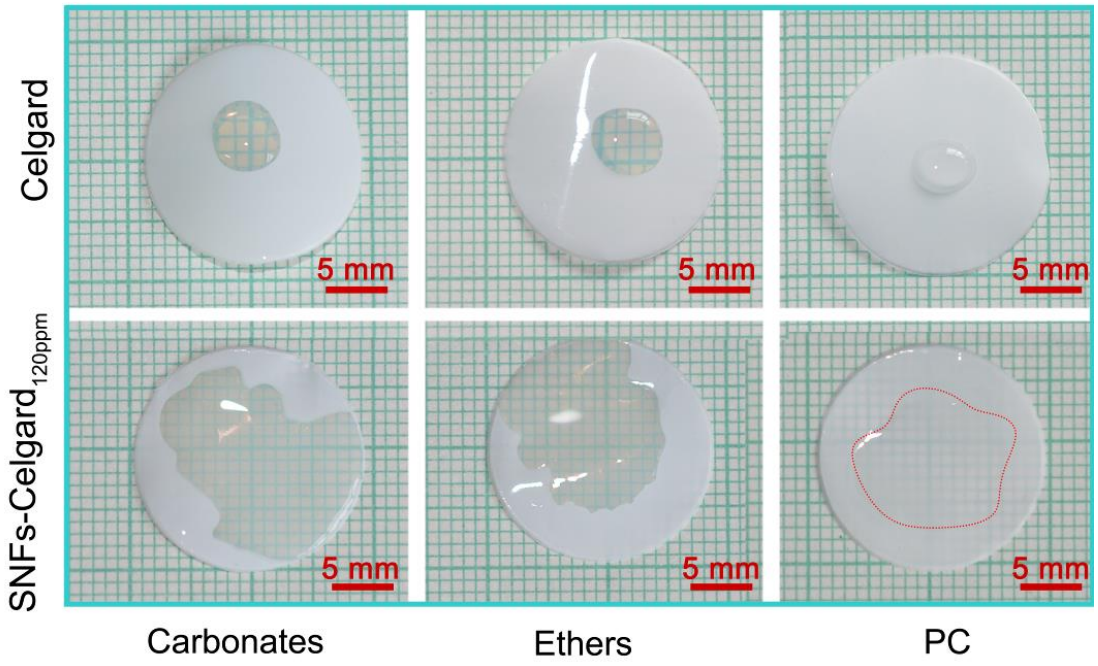

Figure S11. Photographs of wetting behavior of three commonly used LEs with different surface tensions on the surface of the Celgard and SNFs-Celgard$_{120ppm}$ separators, related to Figure 2P.

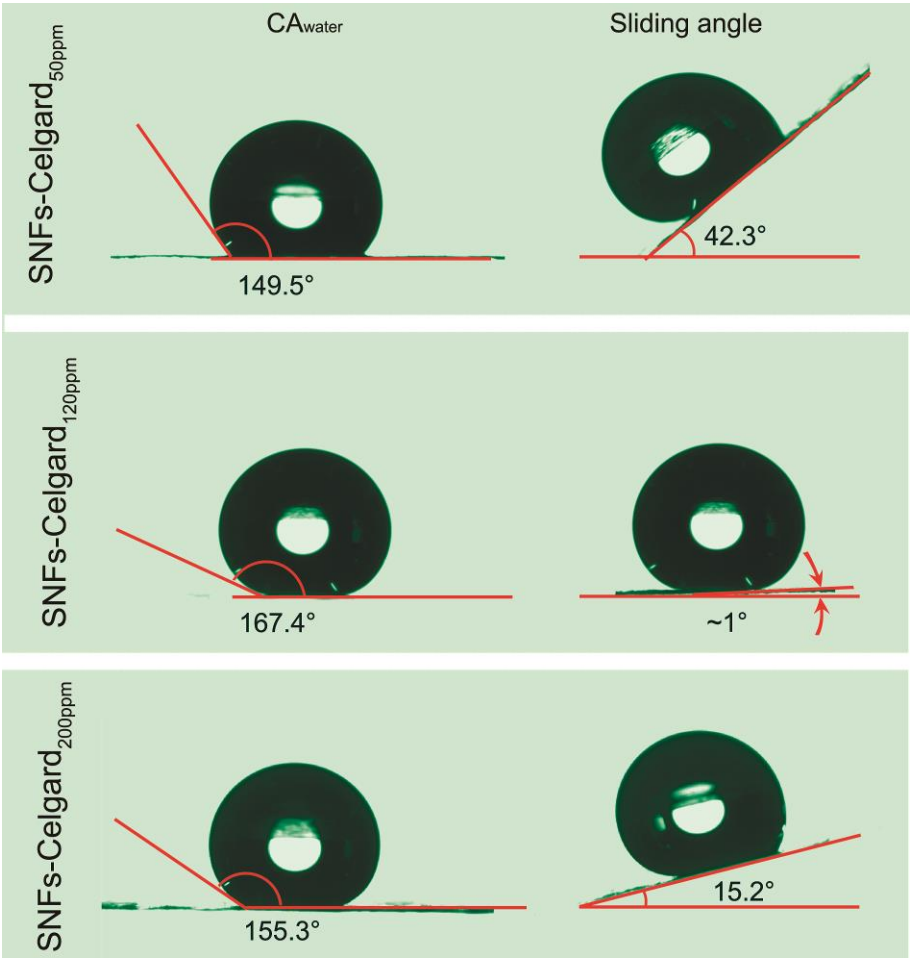

Figure S12. CA_{water} and sliding angle of water on the separators, related to Figure 3A.

Figure S13. Schematic illustration of the device for measuring the moisture uptake of the separators, related to Figure 3C.

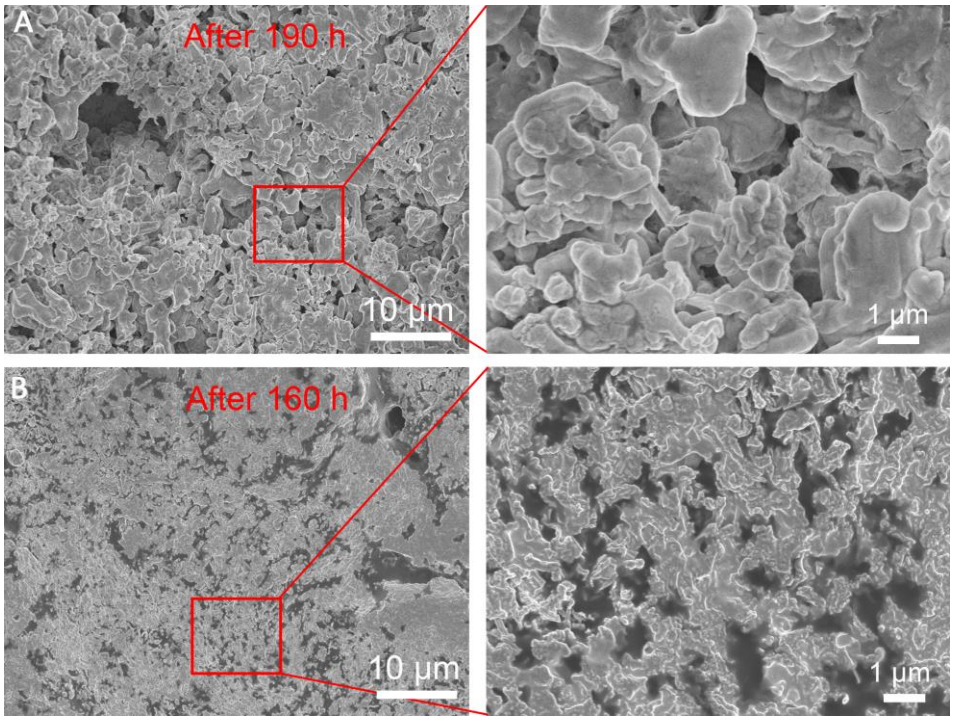

Figure S14. SEM images of the Li anode surface in the Li symmetric cells with (A) Celgard and (B) wet Celgard separators at a current density of 1.0 mA cm^{-2}, related to Figure 3D.

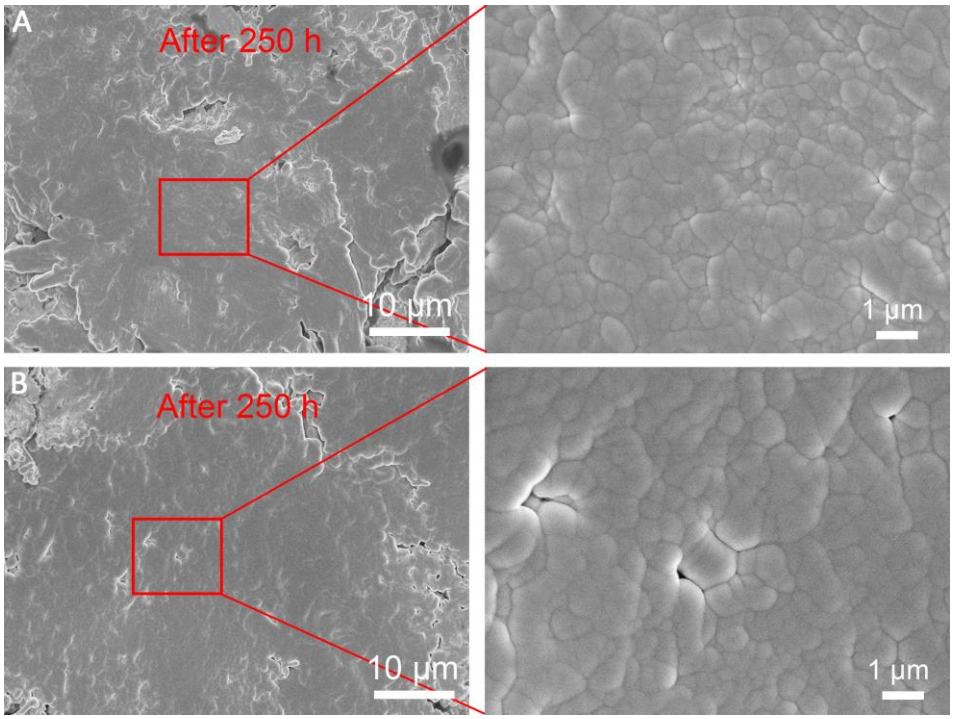

Figure S15. SEM images of the Li anode surface in the Li symmetric cells with (A) SNFs-$Celgard_{120ppm}$ and (B) wet SNFs-$Celgard_{120ppm}$ separators at a current density of 1.0 mA cm^{-2}, related to Figure 3F.

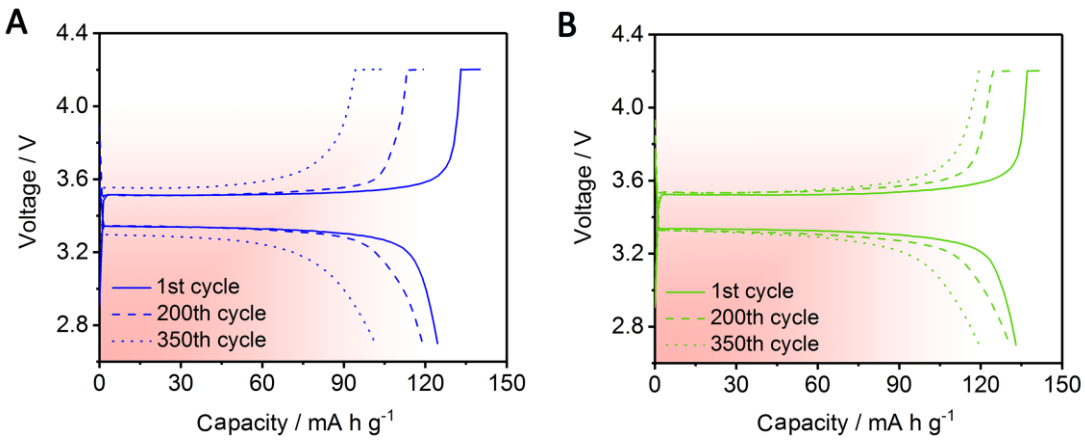

Figure S16. Charge/discharge curves of the Li/$LiFePO_4$ cells with (A) SNFs-$Celgard_{50ppm}$ and (B) SNFs-$Celgard_{200ppm}$ separators, related to Figure 4A.

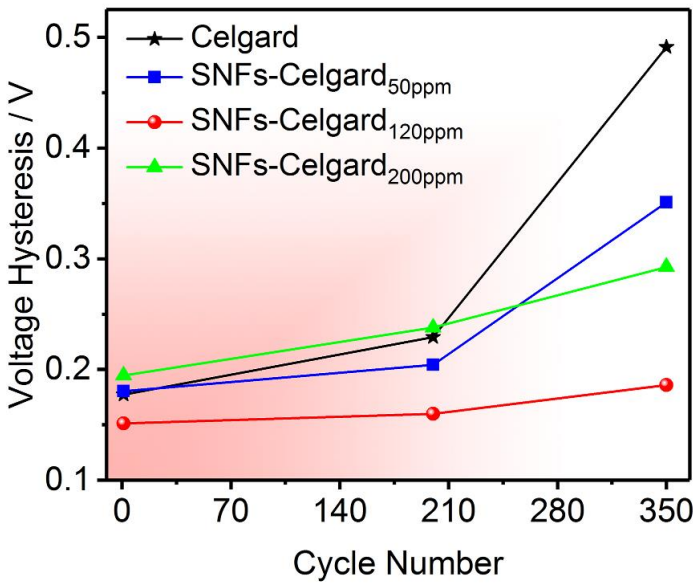

Figure S17. Voltage hysteresis of the Li/$LiFePO_4$ cells with cycle number, related to Figure 4B-C.

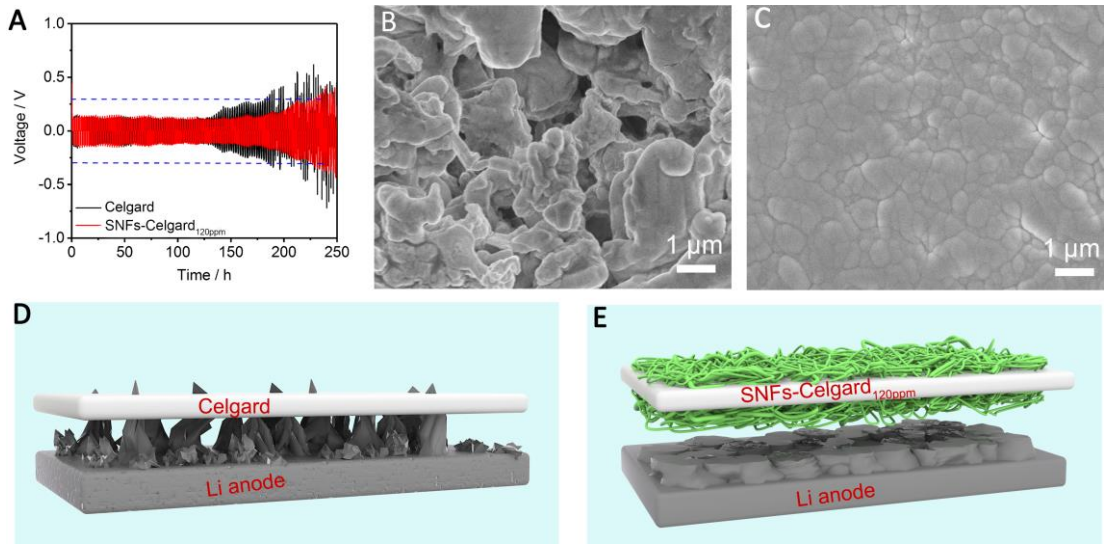

Figure S18. Electrochemical performances of the Li symmetric cells with different separators, related to Figure 4A. (A) Voltage-time curves. SEM images of the Li anode surface in the Li symmetric cells with (B) the Celgard and (C) SNFs-Celgard$_{120ppm}$ separator. The amount of plated Li is 1.0 mAh cm^{-2}, and the current density is 1.0 mA cm^{-2} in each cycle. (D, E) Schematic illustrations of dendrite Li growth with different separators.

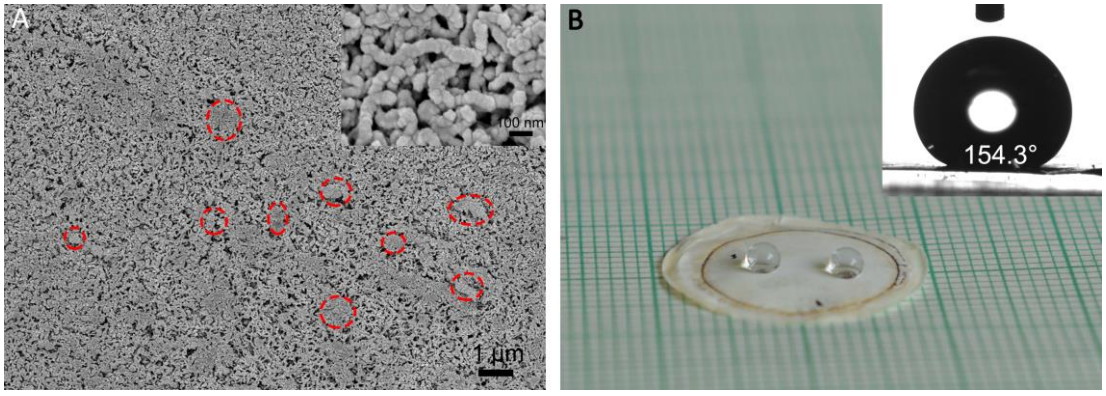

Figure S19. (A) SEM images of the SNFs-Celgard$_{120ppm}$ separator after 350 cycles and (B) photographs of 10 μL water droplets on the SNFs-Celgard$_{120ppm}$ separator after 350 cycles, related to Figure 4.

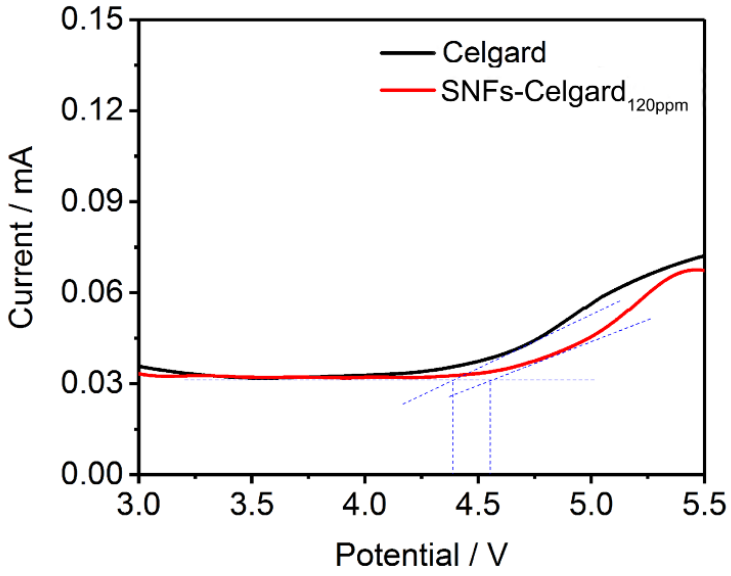

Figure S20. Linear sweep voltammetry profiles of the Celgard and SNFs-Celgard$_{120ppm}$ separators, related to Figure 4.

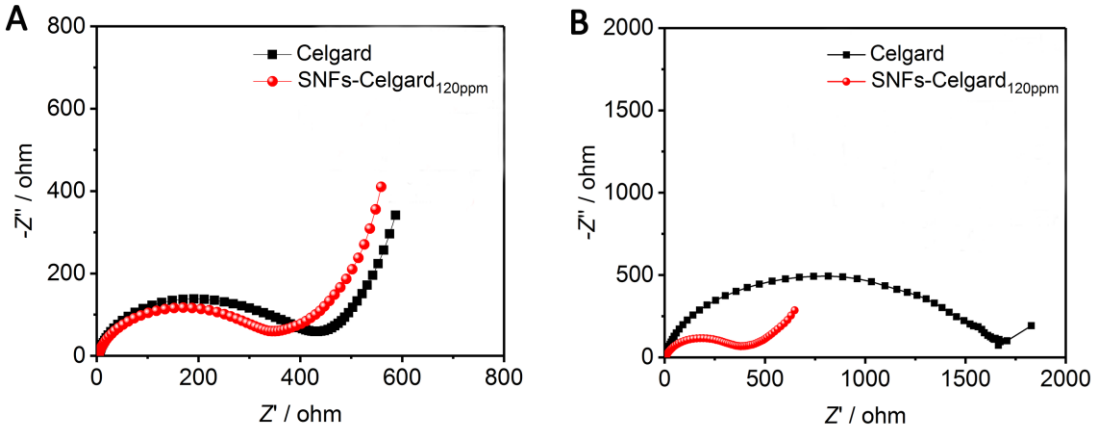

Figure S21. Nyquist plots of the Li/LiFePO$_4$ cells with different separators (A) before cycling and (B) after 100 cycles, related to Figure 4A.

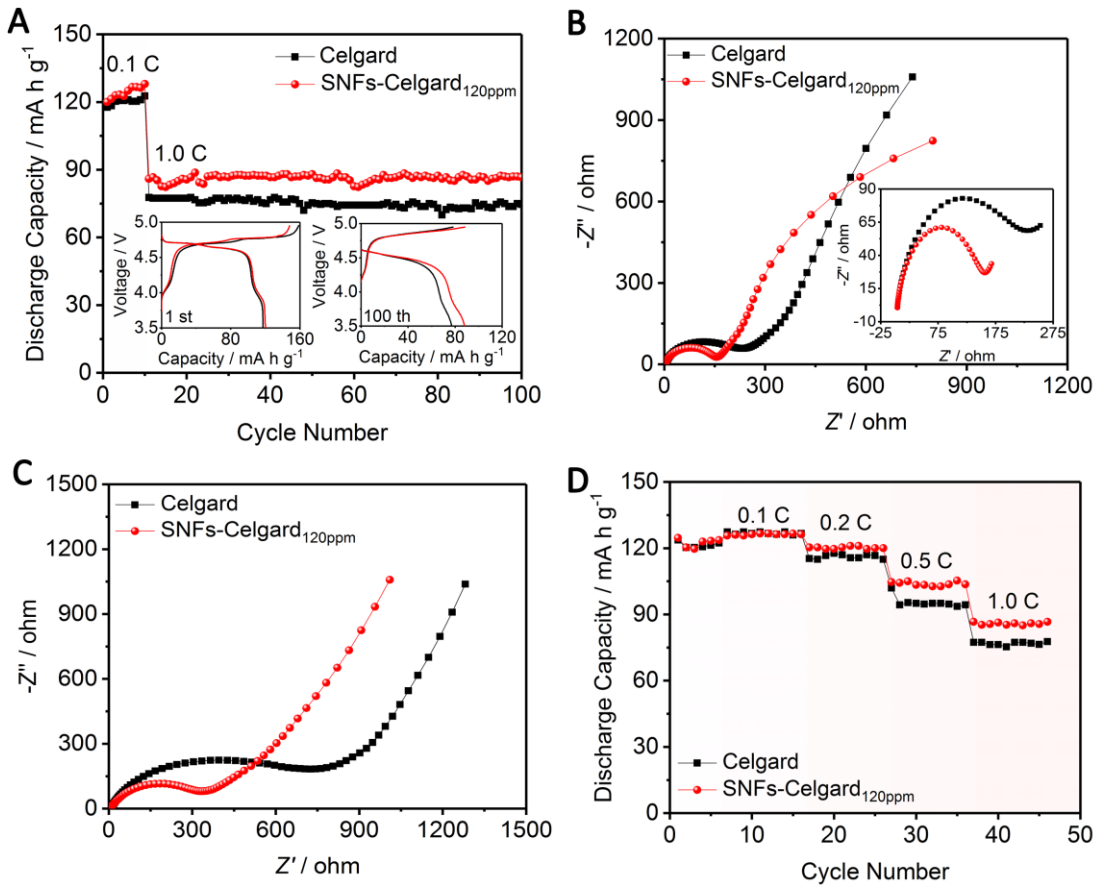

Figure S22. Electrochemical performances of the Li/$LiNi_{0.5}Mn_{1.5}O_4$ cells, related to Figure 4. (A) Cycling stability at 1.0 C (1.0 C = 140 mA h g^{-1}), Nyquist plots (B) before cycling and (C) after 100 cycles, and (D) rate performance. The insets in (A) show discharge/charge profiles.

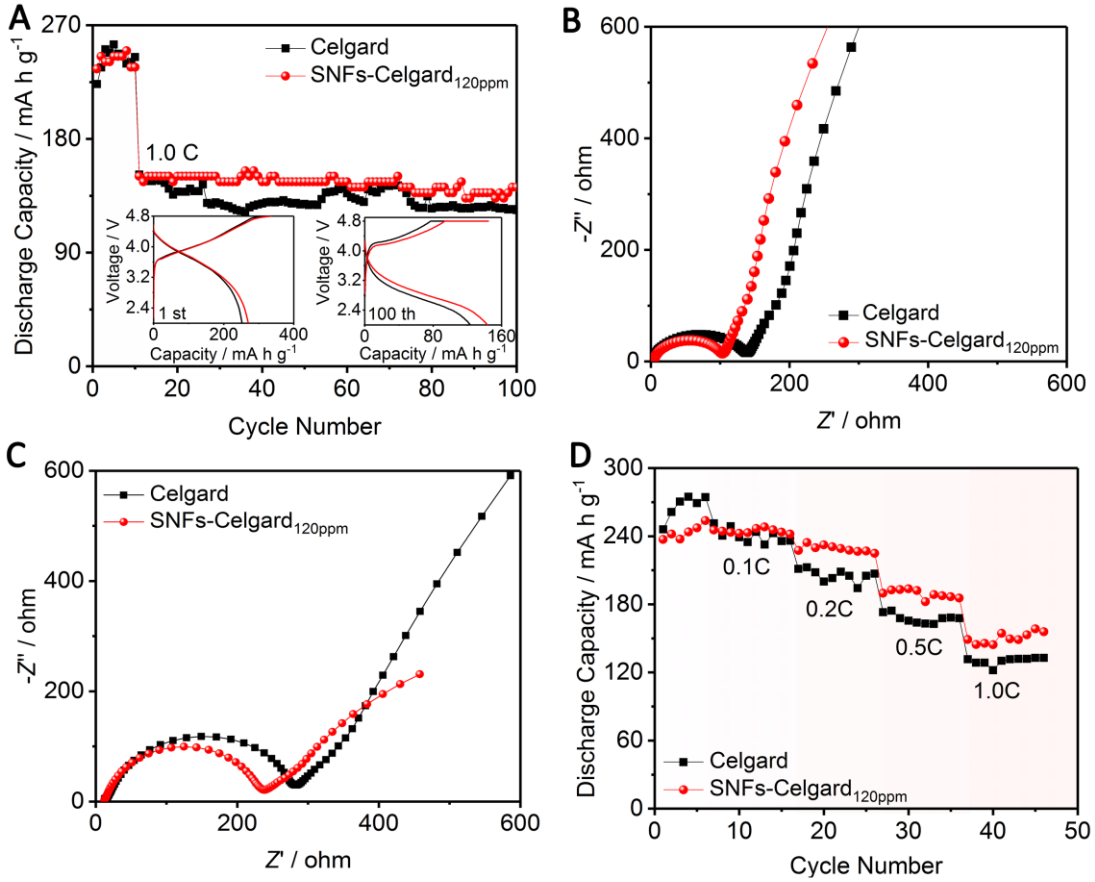

Figure S23. Electrochemical performances of the Li/$Li_{1.2}Mn_{0.54}Ni_{0.3}Co_{0.3}O_2$ cells, related to Figure 4. (A) Cycling stability at 1.0 C (1.0 C = 360 mA h g^{-1}), Nyquist plots (B) before cycling and (C) after 100 cycles, and (D) rate performance. The insets in (A) show discharge/charge profiles.

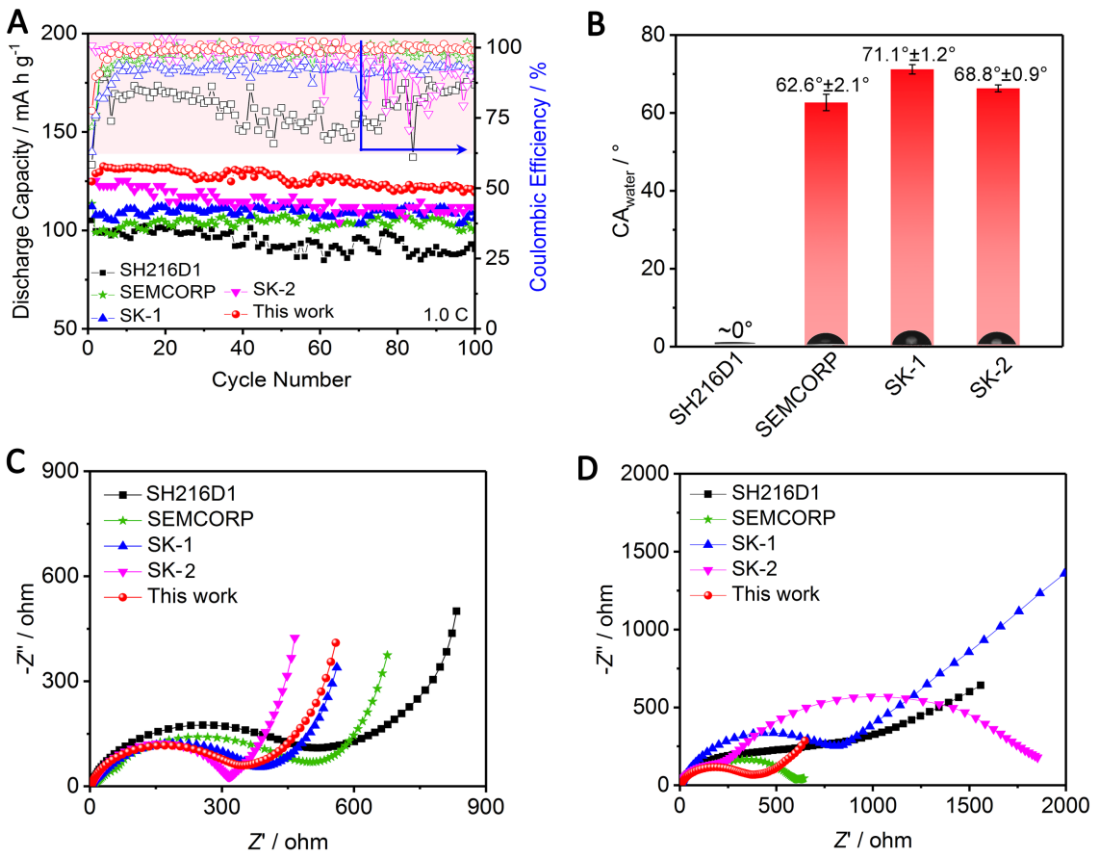

Figure S24. Electrochemical Performances of the Li/$LiFePO_4$ cells with the SNFs-Celgard$_{120ppm}$ and the ceramic coated separators, related to Figure 4. (A) Cycling stability at 1.0 C (1.0 C = 160 mA h g^{-1}), (B) CA_{water} on the ceramic coated separators (shown as means ± SD, n = 6), Nyquist plots of the cells (C) before cycling and (D) after 100 cycles. We chose four commercial ceramic coated separators: (1) SEMCORP (one side Al_2O_3 coated PE membrane with a coating thickness of 4 ± 0.1 μm, Yunnan Energy New Material Co., LTD, China), (2) SH216D1 (one side Al_2O_3 coated PP membrane with a coating thickness of 4±1 μm, Shenzhen Senior Technology Material Co., LTD, China), (3) SK-1 (one side Al_2O_3 coated PE membrane with a coating thickness of 4 ± 0.1 μm SKinnovation, Korea) and (4) SK-2 (double side Al_2O_3 coated PE membrane with a coating thickness of 2 μm on each side, SKinnovation, Korea).

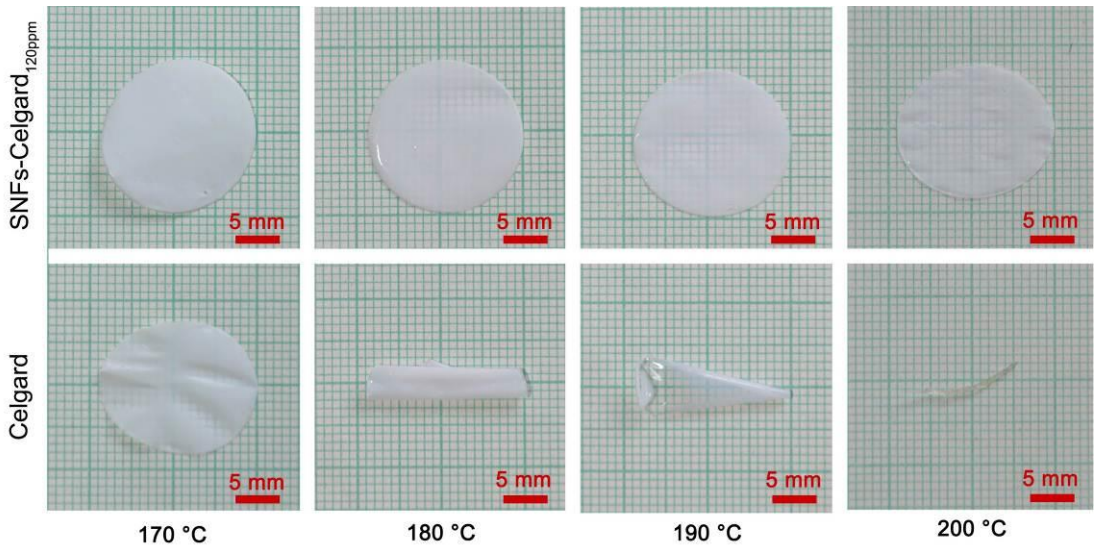

Figure S25. Dimension of the separators before and after heat treatment at different temperature for 1 h, related to Figure 5A.

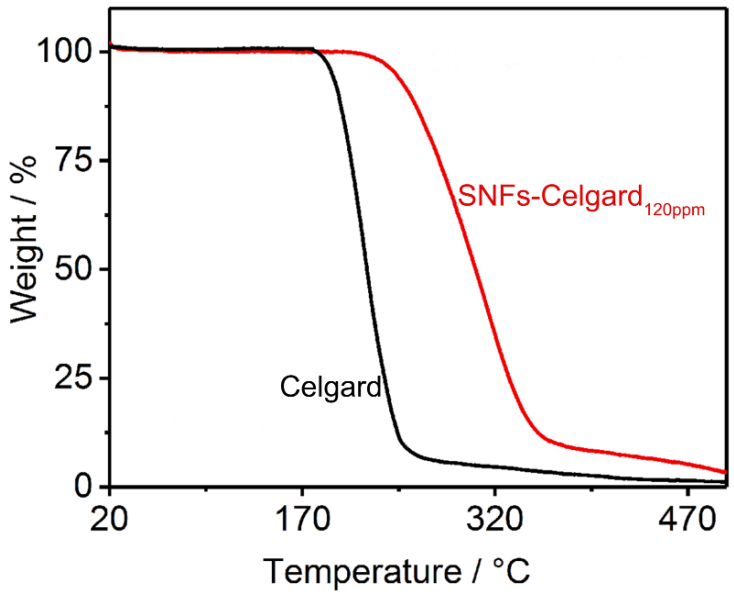

Figure S26. TGA curves of the separators, related to Figure 5.

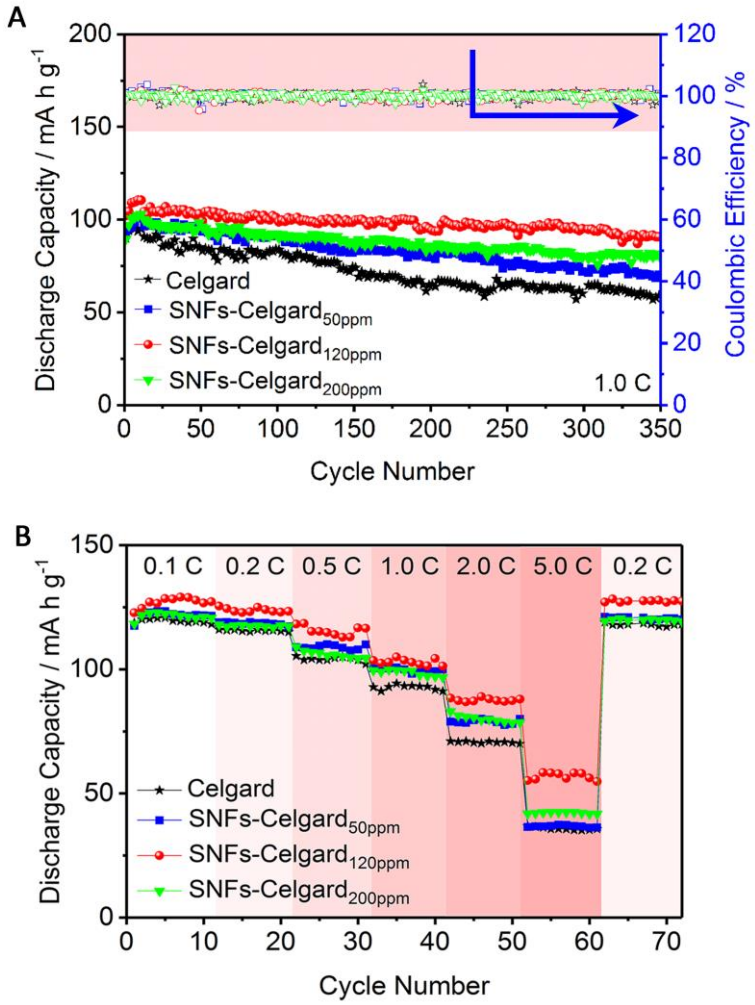

Figure S27. (A) Cycling stability and (B) rate performance of the $LiFePO_4$/graphite cells with different separators (1.0 C = 133 mA h g^{-1}), related to Figure 6.

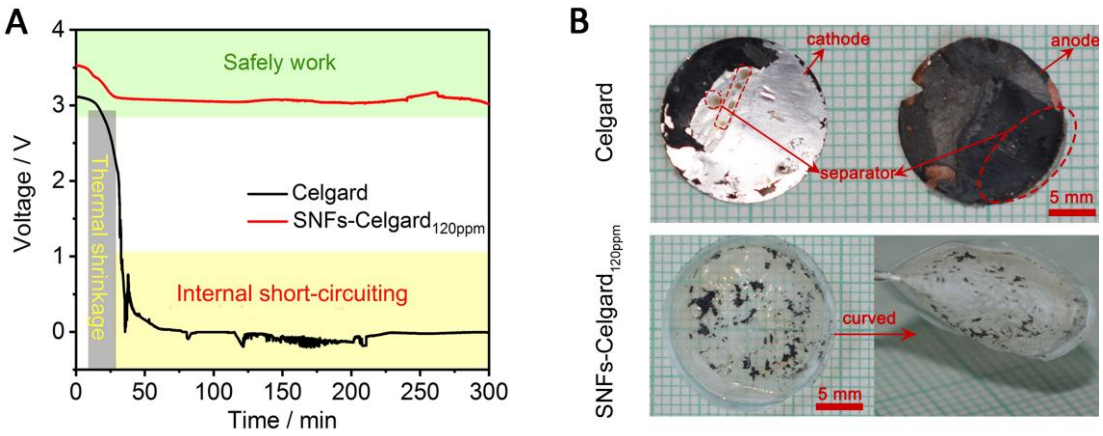

Figure S28. (A) OCV curves of the $LiFePO_4$/graphite cells with different separators at 170 °C. (B) Photographs of the separators after the OCV test, related to Figure 6.

Table S1. Surface tension of various LEs (shown as means ± SD, n = 12), related to Figure 2 and Figure 3.

LEs	Carbonates	Ethers	PC
Surface tension / mN m^{-1}	27.79 ± 0.06	26.56 ± 0.35	31.35 ± 0.16

Table S2. Atomic ratio of O, C and Si on the surface of the SNFs-Celgard$_{120ppm}$ separator, related to Figure 1E and F.

Elements	O	C	Si
Atomic ratio / %	31.55	46.78	21.67

Table S3. Physical and electrochemical parameters of the separators, related to Figure 2.

Separators	Celgard	SNFs-Celgard$_{50ppm}$	SNFs-Celgard$_{120ppm}$	SNFs-Celgard$_{200ppm}$
Porosity / %	44.9	45.7	51.9	47.9
LE uptake / %	91.3	165.5	287.8	196.9
Conductivity / mS cm^{-1}	0.727	0.740	1.02	0.832

Table S4. Wettability of the previously reported separators and the SNFs-Celgard$_{120ppm}$ separator, related to Figure 2 and Figure 3.

Separators	CA_{LE} / °	CA_{water} / °	Ref.
PVDF/ZSM-Si(Al) coated PE	- [a]	14.5	Mao et al., 2017
(PEI/SiO_2) modified PE	-	24.6	Wang et al., 2015
PE-SiO_2@PDA	-	36	Dai et al., 2016
(PAA/ZrO_2)$_3$ modified PE	-	38	Xu et al., 2015
Polydopamine coated PE	-	39	Ryou et al., 2011
N-SiO_2 coated PE	-	51.3	Cho et al., 2017
PAA/PEO@PP	27.8	71.7	Li et al., 2015
Tannic acid coated PP	-	72	Pan et al., 2015
SiO_2 grafted PE	-	79	Zhu et al., 2015
TiO_2 grafted PE	-	89	Zhu et al., 2016
Al_2O_3/LPMA64 coated PE	-	95	Na et al., 2016
Al_2O_3/PI coated PE	0	Hydrophilic [b]	Shi et al., 2016
SiO_2-PMMA coated PE	6.1	hydrophilic	Yang et al., 2015
SiO_2/WCDA coated PE	8	hydrophilic	Chen et al., 2016
Al_2O_3/CGS grafted PE	21	hydrophilic	Jiang et al., 2017
Hydroxyapatite/cellulose fibers	0	hydrophilic	Li et al., 2017
PU	5	hydrophilic	Kim et al., 2016
Chitin nanofibers	9.2	hydrophilic	Zhang et al., 2017
Poly(*p*-phenylene benzobisoxazole)	20	hydrophilic	Hao et al., 2016
PPy@NCFs/NCFs	0	hydrophilic	Wang et al., 2017
SH216D1	4	0	tested [c]
SEMCORP	0	62.6	tested
SK-1	0	71.1	tested
SK-2	8.3	68.8	tested
SNFs-Celgard$_{120ppm}$	**0**	**167.4**	**This work**

a. "-" means not mentioned.

b. "hydrophilic" means that the material for modification of the separators is hydrophilic.

c. "tested" means that the CA of LE and water was measured at 25 °C using 10 μL droplets on a Contact Angle System OCA 20.

Table S5. Cost of the SNFs layer on the SNFs-Celgard separator, related to Figure 1.

Cost of TCMS	Cost of O_2-plasma treatment	Cost of the SNFs layer on the SNFs-Celgard separator
152.5 USD for 2 kg (ABCR)	0.03 USD m^{-2}	0.58 USD m^{-2}
144.0 USD for 2 kg (Gelest)		0.55 USD m^{-2}
10430 USD for 1000 kg (block transaction)		0.11 USD m^{-2}

TRANSPARENT METHODS

Materials

Toluene, ethanol and *n*-hexadecane were purchased from China National Medicines Co., Ltd. TCMS (98%) was purchased from Gelest. $LiFePO_4$, carbon black, graphite, *N*-methyl-2-pyrolidone and PVDF were purchased from Shenzhen Kejing Star Technology Co., Ltd., China. All the LEs were purchased from Zhangjiagang Guotai Huarong Chemical New Material Co., Ltd., China. $LiNi_{0.5}Mn_{1.5}O_4$ and $Li_{1.2}Mn_{0.54}Ni_{0.3}Co_{0.3}O_2$ were provided by Lanzhou University of Technology, China. All chemicals were used as received without further purification.

Preparation of SNFs-Celgard Separators

First, the polyolefin separator (Celgard 2400) was activated with O_2-plasma (HARRICK PLASMA PDC-002, USA) at an O_2 flow rate of 60 sccm and a power of 15 W for 1 min. The SNFs-Celgard separators were prepared using a similar method described in our previous papers (Zhang and Seeger, 2011; Zhang et al., 2014). In brief, a fresh solution containing 80 mL of toluene with certain water concentrations (50, 120, and 200 ppm) and 50 µL of TCMS was prepared in a media bottle. Subsequently, a piece of the O_2-plasma activated Celgard separator (68.75 cm^2) was immersed in the solution at room temperature. 6 h later, the SNFs-Celgard separator was successfully prepared. The separator was successively rinsed with 10.0 mL of toluene, 10.0 mL of ethanol and 10 mL of water/ethanol mixture (1:1, v/v), and then dried at 30 °C.

Measurements of Wetting Behaviors

To investigate wettability of the separators, the CA of water and LEs was collected at 25 °C using 10 µL droplets on a Contact Angle System OCA 20 (Dataphysics, Germany). It should be noted that the LE refers to the carbonates based LE (1 M $LiPF_6$ in 1:1 (v/v) EC and DMC) if not specified. The surface tension of various LEs was measured at 25 °C using 10 µL droplets on a Contact Angle System DSA100 (KRÜSS,

Germany). The dynamic wetting behavior of the separators was tested at 4000 fps using a high-speed digital camera (FASTCAM Mini UX100, Photron, Japan).

Measurements of LE Uptake and Moisture Uptake

The LE uptake of the separators was measured by soaking the separators in the LE for 2 h. Subsequently, the separators were taken out of the LE, and the excess LE on the surface of the separator was removed by wiping with filter paper. The LE uptake was calculated using formula (Dai et al., 2016):

$$\text{LE uptake (\%)} = (m_2\text{-}m_1)/m_1 \times 100\% \quad (1)$$

where m_1 and m_2 are the weight of the separators before and after LE absorption, respectively.

To measure the moisture uptake of the separators, the separators were dried at 60 °C for 24 h in a vacuum oven to a constant weight. Subsequently, the separators were put into a chamber with a constant relative humidity of 92.6% at 25 °C for 7 days (Figure S13). The moisture uptake was calculated using formula (Mihranyan et al., 2004; Peng et al., 2013):

$$\text{Moisture uptake (\%)} = (m_4\text{-}m_3)/m_3 \times 100\% \quad (2)$$

where m_3 is the weight of the dry separators, and m_4 is the weight of conditioned separators (termed as wet ones). In order to study the effect of moisture uptake on performance of the separators, the separators after moisture uptake test were immediately used for assembly of Li symmetric cells.

Electrode Preparation

To preparation the $LiFePO_4$ cathode, the $LiFePO_4$ powder was mixed with 10 wt% PVDF and 10 wt% super P in *N*-methyl-2-pyrolidone to form the active material slurry. The slurry was coated on Al foil by the tape casting method. The cathode was dried in a vacuum oven at 60 °C for 24 h, compressed, and cut into circular disks. The content of the active material in each cathode circular disk is 2.6 mg cm^{-2}. The high voltage $LiNi_{0.5}Mn_{1.5}O_4$ and $Li_{1.2}Mn_{0.54}Ni_{0.3}Co_{0.3}O_2$ cathodes were prepared via a similar process. The $LiNi_{0.5}Mn_{1.5}O_4$ and $Li_{1.2}Mn_{0.54}Ni_{0.3}Co_{0.3}O_2$ contents in the

cathodes are 2.0 mg cm^{-2}. The graphite anode was prepared via a similar process, except that the carboxymethylcellulose was used as a binder and the slurry was coated on copper foil. The content of graphite in each anode circular disk is 4.5 mg cm^{-2}.

Cell Assembly and Electrochemical Tests

CR2032 coin cells were used for all cell assembly and electrochemical tests. 50 µL of the LE was used in each cell. All the procedures were carried out in an Ar-filled glovebox with O_2 and water contents below 0.1 ppm. The Li symmetrical cells were assembled by sandwiching a separator between two Li electrodes. The performance of the Li symmetric cells was recorded using a CT2001A battery test system (LAND Electronic Co., Ltd. China) at 1 mA cm^{-2} and the amount of plated Li is 1.0 mA h cm^{-2}. For the Li metal cells, the $LiFePO_4$, $LiNi_{0.5}Mn_{1.5}O_4$ and $Li_{1.2}Mn_{0.54}Ni_{0.3}Co_{0.3}O_2$ cathodes, and the separators were dried at 60 °C for 2 h in a vacuum oven prior to cell assembly, and the cells were assembled using different cathodes and Li anode with the separators. The $LiFePO_4$/graphite cells were assembled using $LiFePO_4$ cathode and graphite anode with the separators. The pouch cells were assembled using $LiFePO_4$ cathode and graphite anode. The areal electrode loading and size of the cathode were 15.4 mg cm^{-2} (2.0 mA h cm^{-2}) and 20 cm^2 (4 cm × 5 cm), respectively. The assembled cells were aged at room temperature for 24 h before testing. The discharge/charge and cycling data were recorded using a CT2001A battery test system with a certain voltage window at various cycling rate. The voltage window is 2.7-4.2 V for the Li/$LiFePO_4$ cells, 3.0-4.9 V for the Li/$LiNi_{0.5}Mn_{1.5}O_4$ cells, 2.4-4.8 V for the Li/$Li_{1.2}Mn_{0.54}Ni_{0.3}Co_{0.3}O_2$ cells and 2.4-3.7 V for the $LiFePO_4$/graphite cells.

The electrochemical stability of the separators was evaluated using linear sweep voltammetry (CHI660E, Chenhua Instruments Co., China) from 3.0 to 5.0 V (vs. Li/Li^+) at a scan of 1 mV s^{-1}. The cell was assembled by sandwiching a separator between stainless steel (working electrode) and Li metal (reference and counter electrodes). The Li^+ conductivity of the separators was calculated by the electrochemical impedance spectroscopy (EIS). The cells were assembled by sandwiching a separator

between two stainless steel blocking electrodes. The EIS measurements were carried out using an impedance analyzer (CHI660E) at open circuit potential with a constant perturbation amplitude of 5 mV in the frequency range of 0.1-100 KHz, and was calculated using formula (Yang and Zhang, 2018):

$$\sigma = L/(R_b \times A_1) \quad (3)$$

where σ is the Li^+ conductivity (mS cm^{-1}), L is the thickness of the separator (cm), R_b is the bulk resistance (Ω), and A_1 is the area of the stainless steel electrode (cm^2).

The Li^+ transference number (t_{Li}) of the separators was measured by a potentiostatic polarization method with a constant potential at 20 mV for 1000 s, and was calculated using formula (He et al., 2018):

$$t_{Li} = I_s (\Delta V - I_o R_o)/I_o(\Delta V - I_s R_s) \quad (4)$$

where ΔV is the potentiostatic potential (V); I_o and I_s are the current at initial and steady state (mA), respectively; R_o and R_s are the resistance before and after the potentiostatic polarization (Ω), respectively.

In order to study the safety performance of the cells with different separators at high temperature, the open circuit voltage (OCV) measurement was carried out. The cells were assembled using $LiFePO_4$ cathode and Li anode or graphite anode with different separators. The cell was charged to 4.0 V at 25 °C, and then put into an oven at certain temperature. Subsequently, variation of the voltage with time was monitored using an electrochemical working station (CHI660E).

Characterization

Surface morphology of the separators was observed via field emission scanning electron microscopy (SEM, JSM-6701F, JEOL). Fourier transform infrared (FTIR) spectra of the separators were collected using a Nicolet NEXUS FTIR spectrometer using KBr pellets. X-ray photoelectron spectra (XPS) of the separators were recorded using a VG ESCALAB 250 Xi spectrometer with a monochromated Al K_α X-ray radiation source and a hemispherical electron analyzer. The spectra were collected in the constant pass energy mode with a value of 100 eV, and all binding energies were calibrated using the C 1s peak at 284.6 eV as the reference. The porosity of the

separators was measured by soaking the separators in *n*-hexadecane for 2 h, and supposing that the pore volume of the separator is equal to the volume of the absorbed *n*-hexadecane by the separator (Dai et al., 2016). The excess *n*-hexadecane on the surface of the separator was removed by wiping with filter paper. The porosity was calculated using formula 5:

$$\text{Porosity}\ (\%) = (\Delta m/\rho)/V_o \quad (5)$$

where Δm is the mass difference of the separator before and after immersion in *n*-hexadecane, V_o is the total volume of the separator, and ρ is the density of *n*-hexadecane.

In order to study thermostability of the separators, the thermal shrinkage was measured based on the area change of the separator (2.83 cm^2 circle) before and after heat treatment at certain temperature (120-200 °C) for 1 h, and was calculated using formula 6:

$$\text{Thermal shrinkage}\ (\%) = (A_1\text{-}A_2)/A_1 \times 100\% \quad (6)$$

where A_1 and A_2 are the areas of the separator before and after heat treatment, respectively. The thermostability was also analyzed by differential scanning calorimetry (DSC) and thermal gravimetric analysis (TGA) at a heating rate of 10 °C min^{-1} from 20 to 500 °C in O_2 atmosphere.

SUPPLEMENTAL REFERENCES

Chen, W., Shi, L., Zhou, H., Zhu, J., Wang, Z., Mao, X., Chi, M., Sun, L., and Yuan, S. (2016). Water-based organic-inorganic hybrid coating for a high-performance separator. ACS Sus. Chem. Eng. *4*, 3794-3802.

Cho, J., Jung, Y.C., Lee, Y.S., and Kim, D.W. (2017). High performance separator coated with amino-functionalized SiO_2 particles for safety enhanced lithium-ion batteries. J. Membr. Sci. *535*, 151-157.

Dai, J., Shi, C., Li, C., Shen, X., Peng, L., Wu, D., Sun, D., Zhang, P., and Zhao, J. (2016). A rational design of separator with substantially enhanced thermal features for lithium-ion batteries by the polydopamine-ceramic composite modification of polyolefin membranes. Energy Environ. Sci. *9*, 3252-3261.

Hao, X., Zhu, J., Jiang, X., Wu, H., Qiao, J., Sun, W., Wang, Z., and Sun, K. (2016). Ultrastrong polyoxyzole nanofiber membranes for dendrite-proof and heat-resistant battery separators. Nano Lett. *16*, 2981-2987.

He, Y., Chang, Z., Wu, S., Qiao, Y., Bai, S., Jiang, K., He, P., and Zhou, H. (2018). Simultaneously inhibiting lithium dendrites growth and polysulfides shuttle by a flexible MOF-based membrane in Li-S batteries. Adv. Energy Mater. *8*, 1802130.

Jiang, X., Zhu, X., Ai, X., Yang, H., and Cao, Y. (2017). Novel ceramic-grafted separator with highly thermal stability for safe lithium-ion batteries. ACS Appl. Mater. Interfaces *9*, 25970-25975.

Kim, B.G., Kim, J.S., Min, J., Lee, Y.H., Choi, J.H., Jang, M.C., Freunberger, S.A., and Choi, J.W. (2016). A moisture- and oxygen-impermeable separator for aprotic Li-O_2 batteries. Adv. Funct. Mater. *26*, 1747-1756.

Li, B., Li, Y., Dai, D., Chang, K., Tang, H., Chang, Z., Wang, C., Yuan, X.Z., and Wang, H. (2015). Facile and nonradiation pretreated membrane as a high conductive separator for Li-Ion batteries. ACS Appl. Mater. Interfaces *7*, 20184-20189.

Li, H., Wu, D., Wu, J., Dong, L.Y., Zhu, Y.J., and Hu, X. (2017). Flexible, high-wettability and fire-resistant separators based on hydroxyapatite nanowires for advanced lithium-ion batteries. Adv. Mater. *29*, 170354.

Mao, X., Shi, L., Zhang, H., Wang, Z., Zhu, J., Qiu, Z., Zhao, Y., Zhang, M., and Yuan, S. (2017). Polyethylene separator activated by hybrid coating improving Li^+ ion transference number and ionic conductivity for Li-metal battery. J. Power Sources *342*, 816-824.

Mihranyan, A., Llagostera, A.P., Karmhag, R., Strømme, M., and Ek, R. (2004). Moisture sorption by cellulose powders of varying crystallinity. Inter. J. Phar. *269*, 433-442.

Na, W., Lee, A.S., Lee, J.H., Hwang, S.S., Kim, E., Hong, S.M., and Koo, C.M. (2016). Lithium dendrite suppression with UV-curable polysilsesquioxane separator binders. ACS Appl. Mater. Interfaces *8*, 12852-12858.

Pan, L., Wang, H., Wu, C., Liao, C., and Li, L. (2015). Tannic-acid-coated polypropylene membrane as a separator for lithium-ion batteries. ACS Appl. Mater. Interfaces *7*, 16003-16010.

Peng, J.H., Bi, H.T., Lim, C.J., and Sokhansanj, S. (2013). Study on density, hardness, and moisture uptake of torrefied wood pellets. Energy Fuels *27*, 967-974.

Ryou, M.H., Lee, Y.M., Park, J.K., and Choi, J.W. (2011). Mussel-inspired polydopamine-treated polyethylene separators for high-power Li-ion batteries. Adv. Mater. *23*, 3066-3070.

Shi, C., Dai, J., Shen, X., Peng, L., Li, C., Wang, X., Zhang, P., and Zhao, J. (2016). A high-temperature stable ceramic-coated separator prepared with polyimide binder/Al_2O_3 particles for lithium-ion batteries. J. Membr. Sci. *517*, 91-99.

Wang, Z., Guo, F., Chen, C., Shi, L., Yuan, S., Sun, L., and Zhu, J. (2015). Self-assembly

of PEI/SiO_2 on polyethylene separators for Li-ion batteries with enhanced rate capability. ACS Appl. Mater. Interfaces *7*, 3314-3322.

Wang, Z., Pan, R., Ruan, C., Edström, K., Strømme, M., and Nyholm, L. (2017). Redox-active separators for lithium-ion batteries. Adv. Sci., 1700663.

Xu, W., Wang, Z., Shi, L., Ma, Y., Yuan, S., Sun, L., Zhao, Y., Zhang, M., and Zhu, J. (2015). Layer-by-layer deposition of organic-inorganic hybrid multilayer on microporous polyethylene separator to enhance the electrochemical performance of lithium-ion battery. ACS Appl. Mater. Interfaces *7*, 20678-20686.

Yang, P., Zhang, P., Shi, C., Chen, L., Dai, J., and Zhao, J. (2015). The functional separator coated with core-shell structured silica-poly(methyl methacrylate) sub-microspheres for lithium-ion batteries. J. Membr. Sci. *474*, 148-155.

Yang, Y., and Zhang, J. (2018). Highly stable lithium-sulfur batteries based on laponite nanosheet-coated celgard separators. Adv. Energy Mater. *8*, 1801778.

Zhang, J., and Seeger, S. (2011). Superoleophobic coatings with ultralow sliding angles based on silicone nanofilaments. Angew. Chem. Int. Ed. *50*, 6652-6656.

Zhang, J., Wang, A., and Seeger, S. (2014). *Nepenthes* pitcher inspired anti-wetting silicone nanofilaments coatings: preparation, unique anti-wetting and self-cleaning behaviors. Adv. Funct. Mater. *24*, 1074-1080.

Zhang, T.W., Shen, B., Yao, H.B., Ma, T., Lu, L.L., Zhou, F., and Yu, S.H. (2017). Prawn shell derived chitin nanofiber membranes as advanced sustainable separators for Li/Na-Ion batteries. Nano Lett. *17*, 4894-4901.

Zhu, X., Jiang, X., Ai, X., Yang, H., and Cao, Y. (2015). A highly thermostable ceramic-grafted microporous polyethylene separator for safer lithium-ion batteries. ACS Appl. Mater. Interfaces *7*, 24119-24126.

Zhu, X., Jiang, X., Ai, X., Yang, H., and Cao, Y. (2016). TiO_2 ceramic-grafted

polyethylene separators for enhanced thermostability and electrochemical performance of lithium-ion batteries. J. Membr. Sci. *504*, 97-103.